Dynamics of a helical swimmer crossing viscosity gradients

Christian Esparza López,[1] Jorge Gonzalez-Gutierrez,[2,3] Francisco Solorio-Ordaz,[3] Eric Lauga,[1,*] and Roberto Zenit[4,5,†]

[1]*Department of Applied Mathematics and Theoretical Physics, University of Cambridge, Cambridge CB3 0WA, United Kingdom*

[2]*Facultad de Ciencias en Física y Matemáticas Universidad Autónoma de Chiapas, Tuxtla Gutiérrez, Chiapas, Mexico*

[3]*Departamento de Termofluidos, Facultad de Ingeniería, Universidad Nacional Autanoma de México, Av. Universidad 3000, Ciudad de México, 04510, Mexico*

[4]*Instituto de Investigaciones en Materiales, Facultad de Ingeniería, Universidad Nacional Autnoma de México, Av. Universidad 3000, Ciudad de México, 04510, Mexico*

[5]*School of Engineering, Brown University, 184 Hope St., Providence, Rhode Island 02912, USA*

(Received 9 December 2020; accepted 20 July 2021; published 23 August 2021)

We experimentally and theoretically study the dynamics of a low-Reynolds number helical swimmer moving across viscosity gradients. Experimentally, a double-layer viscosity is generated by superposing two miscible fluids with similar densities but different dynamic viscosities. A synthetic helical magnetically driven swimmer is then made to move across the viscosity gradients along four different configurations: either head-first (pusher swimmer) or tail-first (puller), and through either positive (i.e., going from low to high viscosity) or negative viscosity gradients. We observe qualitative differences in the penetration dynamics for each case. We find that the swimming speed can either increase or decrease while swimming across the viscosity interface, which results from the fact that the head and the tail of the swimmer can be in environments in which the local viscosity leads to different relative amounts of drag and thrust. In order to rationalize the experimental measurements, we next develop a theoretical hydrodynamic model. We assume that the classical resistive-force theory of slender filaments is locally valid along the helical propeller and use it to calculate the swimming speed as a function of the position of the swimmer relative to the fluid-fluid interface. The predictions of the model agree well with experiments for the case of positive viscosity gradients. When crossing across a negative gradient, gravitational forces in the experiment become important, and we modify the model to include buoyancy, which agrees with experiments. In general our results show that it is harder for a pusher swimmer to cross from low to high viscosity, whereas for a puller swimmer it is the opposite. Our model is also extended to the case of a swimmer crossing a continuous viscosity gradient.

DOI: 10.1103/PhysRevFluids.6.083102

I. INTRODUCTION

Taxis is the capability of biological cells to respond to an external stimulus, such as a light or chemical gradients, and as a result move towards or away from it [1]. In nature, the adaptability of microorganisms to respond to a variety of cues has been demonstrated in gradients of light

*e.lauga@damtp.cam.ac.uk
†zenit@brown.edu

intensity (phototaxis) [2–6], magnetic fields (magnetotaxis) [7–9], temperature (thermotaxis) [10–12], gravitational potential (gravitaxis) [13–15], and chemical stimuli (chemotaxis) [16].

For many motile microorganisms, chemotaxis is a crucial method to escape from toxins (chemo-repulsion or negative chemotaxis) and to find sources of food (chemo-attraction or positive chemotaxis). Two illustrative examples are the well-studied bacterium *Escherichia coli* [17], whose study is at the heart of most of what we know about bacterial sensing and information processing, and spermatozoa looking for the ovum during fertilization [18]. Beyond individual behavior, microorganisms may also exhibit collective dynamics through chemically based communication. For example, when a *Dictyostelium* cell (a type of mold) starves, it produces a chemical that induces a multicellular aggregation process, which allows the cells to survive long starvation periods [16,19–21]. The mechanism behind this phenomenon is captured in the classical Keller-Segel model [22,23] and has been extended to describe some collective phenomena of *E. coli* bacteria showing chemo-attraction to self-produced autoinducers [24].

A mechanical example of taxis, viscotaxis, emerges when a cell adapts its motion in response to viscosity gradients. Some microorganisms, such as *Spiroplasma* [25] and *Leptospira interrogans* [26–28], have indeed the ability to respond to changes in viscosity. A particularly important example for human health is the colonization of the stomach by the bacterium *Helicobacter pylori*, which turns out to be another consequence of the ability to move in viscosity gradients [29,30]. Indeed, *H. pylori* is the only known bacteria to be capable of penetrating the intestinal mucus layer and reach the stomach wall [29,30], due to an enzymatic degradation of the stomach mucosa [31,32]. This leads to severe inflammation that can result in ulcerogenesis or neoplasia, and since the bacterium infects about 50% of the human population it is important to understand its pathogenesis [33].

In this paper we focus on the mechanics of artificial bacteria in model systems displaying gradients in viscosity. In nature, the motion of helicoidal bacteria through a liquid environment is subject to a number of additional physicochemical processes, including screened electrostatics, the interactions with diffusing chemicals, and biochemical noise [34]. From the point of view of continuum fluid mechanics, the dynamics of flagellated bacteria always takes place in the Stokesian regime since the typical Reynolds numbers range from 10^{-4} to 10^{-2}. The hydrodynamics associated with the movement of such microorganisms is therefore dictated by the predominance of viscous forces and the absence of inertia.

Some understanding already exists on the impact of viscosity gradients on the dynamics of both passive and active (swimming) particles. For example, through cross-streamline migration in viscosity gradients, it is possible to sort soft passive particles in microflows [35]. Heated particles create temperature gradients, which induce local variations in viscosity in the surroundings of the particle [36]. For simple swimmers composed of a small number of active spheres, viscotaxis has been recently shown to arise from a mismatch in the viscous forces acting on the different parts of the swimmer, allowing both positive and negative viscotaxis in Newtonian fluids [37]. Although that mechanism does not account for the possible existence of biological viscoreceptors [38], the positive viscotaxis in *Spiroplasma* [25] and *Leptospira* [26–28] can be explained in these terms.

Using the classical squirmer model microswimmer [39–41], work coupling the concentration of nutrients to the viscosity of the fluid showed qualitative differences in the dynamics of swimming, in contrast to fluids with constant viscosity [42]. The squirmer model has also allowed researchers to study theoretically the effect of weak viscosity gradients on the motion of general spherical swimmers, showing in particular how the swimmer "mode" (i.e., whether the swimmer is a pusher or a puller) is critical in setting the sign of the viscotaxis response [43]. However, and despite a good understanding of locomotion of bacteria in Newtonian fluids [44], a theory that explains how viscosity gradients affect the swimming of helical swimmers is currently not available.

Synthetic microswimmers have often been proposed as one modeling approach to study the motility of microorganisms. Self-phoretic Janus colloids, for example, can be made to move through the generation of chemical, electrostatic, or thermal gradients [45]. These systems have been shown to display similarity with biological chemotaxis, and the Keller-Segel equations for both Janus colloids and chemotactic microorganisms are similar [46–50]. Chemotaxis also plays a significant role

in the formation of dynamic clusters and patterns and synthetic colloid microswimmer suspensions [30,31,45,48,50–53].

Artificial helicoidal swimmers typically consist of a rigid magnetic head fixed to a metallic helical tail [54] in which the whole body is made to rotate by an external magnetic field. Propulsion arises as a result of the chirality of the helical tail, in close analogy to the swimming of flagellated bacteria, e.g., *E. coli* [17]. These types of synthetic swimmers preserve the basic physical characteristics that allow locomotion in low-Re environments, namely, the coupling between rotation and translation for a helical slender filament (here the tail). Under this framework, many control parameters can be explored experimentally to quantify the swimming motion in complex environments [55,56].

Recently, inspired by the process through which *H. pylory* crosses the intestinal mucus layer, we conducted an experimental study on the dynamics of helical swimmers moving through the interface between two immiscible fluids [57]. Depending on the orientation of the swimmer and the different stages of penetration (in particular whether the head or the tail reaches first the interface), the interface was shown to dramatically affect the swimmer. However, interfacial tension is not believed to play a significant role in the mucus zone, where instead high-viscosity gradients are dominant. In this paper we therefore consider the case where the helical swimmer crosses a viscosity interface.

We construct experimentally a stratified solution of two miscible fluids with different viscosities and study the motion of the artificial helical swimmer as it crosses the interface between the fluids. We show that the swimmer slows as it crosses from a region of low to high viscosity head-first (i.e., in the pusher mode) but that it increases its speed when it approaches the interface with its tail-forward (puller mode). In contrast, the swimmer always slows when it moves down the gradient, regardless of its orientation. We then develop a hydrodynamic model to explain our observations. Inspired by a previous study on viscotaxis [37], we assume that the standard Newtonian Stokes drag laws are locally valid, and that the swimming behavior is determined by an instantaneous balance between viscous propulsion and drag. For motion up the viscosity gradient, our model predicts a decrease (resp. increase) in the swimming speed for pusher head-forward (resp. puller tail-forward) orientation, which is consistent with the experimental observations. However, due to the reversibility of Stokes flows, our model would predict the opposite behavior when the swimmer moves down the gradient, in contrast with the experiments. Further analysis of our experiments reveal that when the swimmer moves down the gradient it entrains a portion of the high-viscosity fluid into the low-viscosity region, regardless of its orientation. This drift volume increases the apparent density of the swimmer, thereby slowing it due to gravitational forces. Including a buoyancy term in our model to account for this effect allows the theoretical predictions to come closer to the experimental observations.

The paper is organized as follows. In Sec. II we describe the synthetic swimmer, its characteristic geometrical parameters, and the experimental setup. The experimental results for all four configurations are presented in Sec. III, with a focus on the swimming speed as a function of the swimmer position relative to the fluid interface. The mathematical model for a sharp viscosity gradient is developed in Sec. IV, and its extension for a continuous viscosity profile is presented in Sec. V. We next compare our model with the experimental results in Sec. VI; a modified model that takes into account the fluid entrainment is discussed at the end of this section. Finally we discuss our results in Sec. VII.

II. EXPERIMENTAL SETUP AND MATERIALS

To investigate the mechanics of a synthetic swimmer crossing a layer of variable viscosity, we use the helical swimmer previously developed by our group to study swimming in complex media [55–57]. The helical swimmer, shown schematically in Fig. 1(a), consists of a cylindrical head and a right-handed helical tail, both of which are rigid; pictures of the swimmer are shown in Sec. III. The head of the swimmer contains a small magnet; since the entire setup is exposed to an external

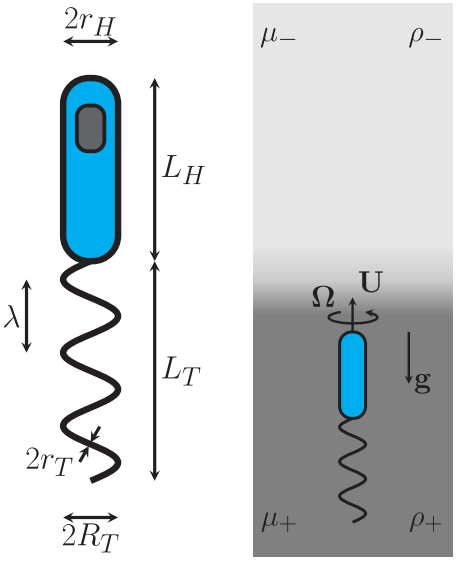

FIG. 1. Experimental setup. (a) Schematic representation of the helical swimmer. The dimensions of the device are $2r_H = 4.5$ mm; $L_H = 16$ mm; $L_T = 16$ mm; $\lambda = 5.3$ mm; $2R_T = 4.5$ mm; and the pitch angle $\psi = 45^\circ$. The thickness of the wire is $2r_T = 0.9$ mm. (b) In this example, the swimmer moves head-first from a high-to-low viscosity fluid through a sharp gradient and here gravity is pointing downwards. Note that in all figures the dark and light gray denote high- and low-viscosity regions, respectively.

magnetic field rotating below the step-out frequency, the swimmer rotates at an imposed rate. Details on the setup can be found in Ref. [58]. With this setup, the speed of the swimmer can be controlled by changing the rotation rate of the external magnetic field, and the swimmer remains force-free throughout. In all experiments reported here, the swimmer moves vertically in either the upwards or downwards direction. Furthermore, the swimming direction (head or tail first) can also be changed: since the helical tail is chiral, reversing the rotation direction of the tail (by changing the rotation direction of the magnetic field) leads to the swimmer moving while either pushing or pulling the head.

A viscosity gradient environment is produced by slowly superposing two miscible viscous liquids onto each other. They are placed, in sequence, in a transparent tank initially leading to a two-layer sharp viscosity gradient, as shown in Fig. 1(b). The bottom liquid is prepared by mixing glucose (530 ml) and water (100 ml) to have a viscosity of approximately $\mu_+ = 2.74$ Pa s, at room temperature. To ensure that the interface remains horizontal, a small amount of salt is added to this liquid (30 g of NaCl) to increase its density slightly, $\rho_+ = 1367.4$ kg/m^3. Note that the slight density stratification helps to maintain the layer stable to conduct several experiments before replacing the fluids. Several combinations of the viscosity gradient are tested, but we report on only one case. The viscosity and density of the top fluid are $\mu_- = 0.55$ Pa s and $\rho_- = 1309.7$ kg/m^3, respectively. The fluid viscosities are measured with a viscometer (DV-III, Brokefield). The densities of the liquids are measured with a 25 ml pycnometer.

The container, with dimensions $8.9 \times 8.9 \times 18$ cm^3, with the swimmer inside is placed within the rotating Helmholtz coil, as in previous experiments [55–57]. To reduce the crystallization of the glucose solutions at the free surface, the container is kept closed at all times. As explained above, the system is slightly density-stratified. Therefore, the swimmer cannot be neutrally buoyant in both top and bottom fluids. The density of the swimmer is adjusted to make it as close as possible to that of the light fluid: $\rho_{\text{swimmer}} \approx 1270$ kg/m^3. Hence, the swimmer is slightly buoyant for both fluids.

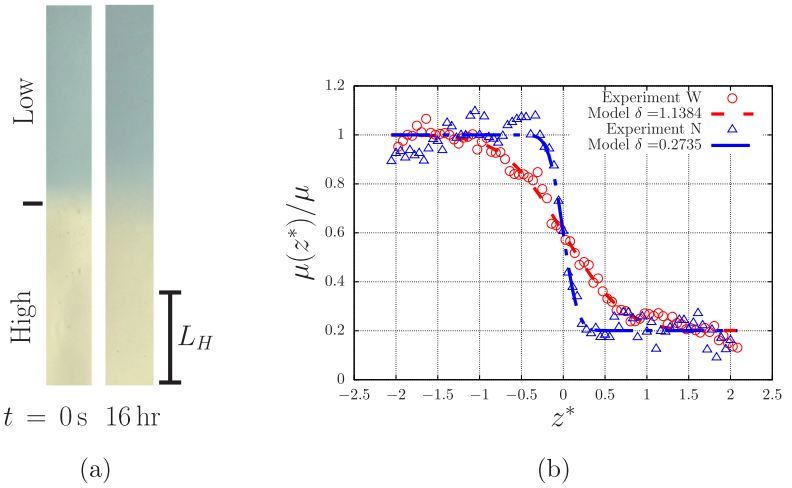

FIG. 2. (a) The viscosity gradients at $t = 0$ and 16 h. (b) Normalized viscosity, $\mu(z)/\mu$, as a function of normalized distance from the interface, $z^* = z/L_H$. Data points represent the pixel intensity, which serves as a proxy for the viscosity profile, soon after the initial setup ($\delta = \Delta/L_H = 0.2735$) and 16 h afterwards ($\delta = 1.1384$). Dashed lines represent the best fit of the Arrhenius equation $\mu(C) = Ae^{BC/C_0}$ with C/C_0 given by Eq. (2), and $A = \mu_-$ and $B = \ln(\mu_+/\mu_-)$.

All experiments are conducted at a fixed rotation rate of the swimmer, $\Omega/2\pi = 2.92$ Hz and the swimmer moves at a constant terminal swimming speed, $U_0 \simeq 1.5$–3.5 mm/s in one of the fluids. Due to the slight density mismatch the terminal speed is different for each fluid and for each direction of motion. The maximum Reynolds number is $\mathrm{Re} = 0.035$, using μ_-, r_H and the maximum swimming speed $U_0 = 3.3$ mm/s, as the characteristic viscosity, length, and speed.

A. Evolution of the viscosity gradient in time

If left undisturbed, the two layers of fluid slowly mix, leading to a diffuse viscosity gradient [Fig. 2(b)]. By conducting experiments at different times after the two-layer fluid is first prepared, the influence of the strength of the viscosity gradient on the swimming process can be tested. The thickness of the viscosity gradient is quantified by applying the following procedure. A dye is added to the low-viscosity gradient, which allows one to track the concentration of glucose and assign a pixel intensity to it. We calculate the concentration gradient along the z-axis at time t by solving the diffusion equation

$$\frac{\partial C}{\partial t} = D\frac{\partial^2 C}{\partial z^2}, \tag{1}$$

where D is the diffusivity and z the distance from the initial interface. Using the Green's function method and the initial distribution $C(z, 0) = C_0[1 - \theta(z)]$, where $\theta(z)$ is the Heaviside step function, we obtain the viscosity distribution as

$$\frac{C(z,t)}{C_0} = \frac{1}{2}\left[1 - \mathrm{erf}\left(\frac{z}{\sqrt{\Delta^2/2}}\right)\right], \tag{2}$$

where $\mathrm{erf}(x)$ is the error function, $\Delta = 2\sqrt{2Dt}$ is the width of the transition region, and C_0 is the initial glucose concentration on the high-viscosity fluid. Next, we assume that the viscosity field μ is related to the concentration C through the Arrhenius equation $\mu(C) = Ae^{BC/C_0}$, where the constants A and B depend on the properties of the fluid mixture [59].

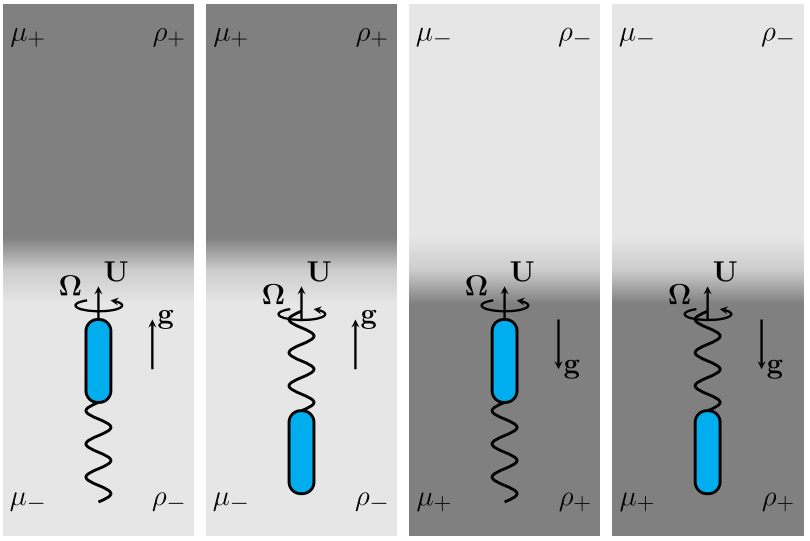

(a) Case I (b) Case II (c) Case III (d) Case IV

FIG. 3. The four swimmer-viscosity interaction configurations for motion across the viscosity gradient. In all cases $\mu_- < \mu_+$ and the motion is in the upwards direction; note that gravity points upwards in (a) and (b) and downwards in (c) and (d). Notice as well the change in the sense of rotation of the tail, depending on its orientation. All conditions are described in Table I.

We show in Fig. 2(b) the resulting viscosity profile obtained experimentally (data points) with the pixel intensity corresponding to the viscosity of each fluid. Here $z = 0$ denotes the position of the fluid interface. The plot is presented in terms of the dimensionless distance $z^* = z/L_H$, where L_H is the length of the head. Negative values of z^* correspond to the bottom fluid, which is more viscous than the high-viscosity fluid located at $z^* > 0$. Choosing A and B so that the viscosity profile matches the initial configuration at $t = 0$, that is, $A = \mu_-$ and $B = \ln(\mu_+/\mu_-)$, we can fit the Arrhenius equation to the experimental data [with C/C_0 given by Eq. (2)] and find the thickness of the transition region $\delta = \Delta/L_H$ as a function of time. The fits are shown in Fig. 2 as dashed lines. In the case where the measurements are conducted soon after the gradient is set up, referred to as a "narrow gradient" (N) in what follows, a value of $\delta = 0.2735$ closely fits the data. For experiments conducted 16 h after the setup, which we will refer to as "wide gradient" (W), the value of $\delta = 1.1384$ closely reproduces the experiments.

It is possible to determine the fluid density, $\rho(z, t)$ in a similar way. Assuming an initial condition $\rho(z) = \rho' + \theta(z)(\rho - \rho')$, an expression analogous to Eq. (2) can be obtained for $\rho(z, t)$.

B. Four different swimmer-viscosity interactions

With the setup described above, we can now consider four distinct swimmer-viscosity interaction scenarios. First, the swimmer can move head-forward (pusher mode) or tail-forward (puller mode). Since the helical tail is chiral, reversing the rotation direction of the tail (by changing the rotation direction of the magnetic field) results, for the same swimmer, in a displacement in the opposite direction. In a uniform fluid at small Re, the swimming speed is, as expected, unaffected by this change of direction (not shown). In addition to the swimming direction, the swimmer can be made to swim across the interface from low to high viscosity (i.e., from μ_- to μ_+) or from high to low viscosity (i.e., from μ_+ to μ_-). These four scenarios are depicted schematically in Fig. 3 and summarized in Table I. In what follows, we will refer to the viscosity gradient as being positive

TABLE I. The four possible swimmer-viscosity interactions depicted in Fig. 3.

Case	Direction	Gradient
I	Head-first (pusher)	Positive
II	Tail-first (puller)	Positive
III	Head-first (pusher)	Negative
IV	Tail-first (puller)	Negative

when the swimmer moves from a low- to a high-viscosity region, or negative in the opposite case, from high to low.

Before each experiment is conducted, the swimmer is slowly placed in the desired initial position and alignment, as far as possible from the interface, such that the viscosity gradient is not significantly disturbed. The motion is recorded with a video camera (920 × 1080 pixels, Sony RX10II, 60 frames per second), using the same distance from the setup to the camera and lens magnification for all experiments. The speed of the swimmer is obtained by measuring its displacement in time. The location of the head is determined using the software TRACKER; the speed is deduced from the position of the head using a central difference scheme. Note that the uncertainty in the measurements of the speed is larger for small swimming speeds, as the displacement must be larger than two pixels between frames. If the traveling time of the swimmer across the two-fluid layer is smaller than the diffusion time, the viscosity gradient can be considered to be approximately constant. Although, in principle, it is possible to conduct experiments considering different values of the viscosity gradient we consider only two cases here: a narrow gradient (N, $\delta = 0.274$) and a wide gradient (W, $\delta = 1.138$), as described above.

III. EXPERIMENTAL RESULTS

We now analyze the crossing of the viscosity gradients by our swimmers along the four configurations described in Table I, for which we find significantly contrasting behaviors. In all experiments, the position z measures the distance from the leading edge of the swimmer to the undisturbed interface; negative and positive z values denote therefore locations before and after reaching the interface, respectively.

A. Case I: Head-first, positive viscosity gradient

In this first case, the swimmer is placed initially at the upper part of the tank. The vertical displacement begins as soon as the rotating magnetic field forces the swimmer to rotate and swim downwards; it reaches quickly its steady-state speed, $U_0^{\mu_-} = 1.75$ mm/s. After the interaction with the interface, the swimmer attains a new steady-state speed $U_0^{\mu_+} = U_+ = 2.5$ mm/s.

In Fig. 4 we show a sequence of images illustrating the crossing process. The time is given in dimensionless terms, $t^* = tU_+/L_H$, and $t^* = 0$ represents the instant at which the swimmer (in this case the head) first reaches the interface. Along with the images, Fig. 5(a) shows the normalized position of the swimmer, $z^* = z/L_H$, as a function of the normalized time, t^* (note that the images have been flipped so that the swimmer appears to move upwards); Fig. 5(b) shows the normalized speed U/U_+ as a function of z^*.

As the swimmer approaches the viscosity gradient, its speed progressively decreases [Figs. 4(a) and 4(b)]. When the head of the swimmer begins to cross the interface [$z^* \approx 0$, Fig. 4(b)], the speed decreases sharply reaching a minimum value at $z^* \approx 0.5$. During this period, the swimming speed is so small that our measurements become inaccurate (they correspond to very small displacement between each frame), characterized by the noisy velocity seen in the region $0.2 < z^* < 1$. Once the head has completely passed, the swimmer experiences two different viscous environments simultaneously: the head is in the high-viscosity region while the tail is in the low-viscosity domain

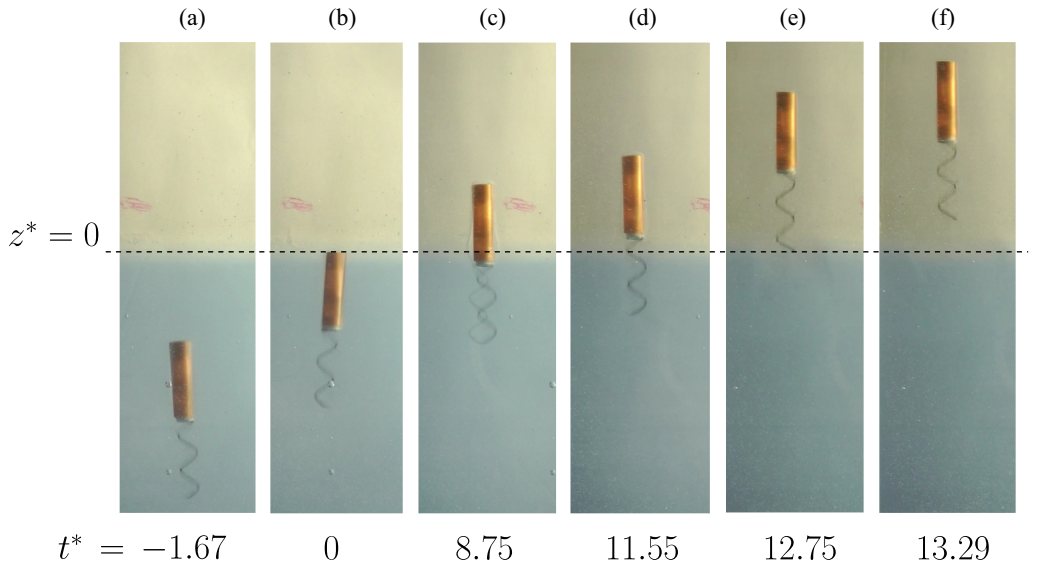

FIG. 4. Case I: time sequence of the head-first (pusher) swimmer crossing a positive viscosity gradient, for $\delta = 0.274$ (narrow gradient). Images have been flipped so that the swimmer appears to move upwards.

[Fig. 4(c)]. Shortly after the head has crossed, the swimmer rapidly increases its speed and the helical tail is progressively crossing the interface [Fig. 4(d)]. Once the tail has completely gone through the interface, the swimmer attains its new steady-state speed, $z^* > 2$ [Figs. 4(e) and 4(f)]. For the two values considered experimentally, the thickness of the viscosity gradient does not seem to affect the process significantly. However, we note that when the gradient is sharp, the swimmer spends a longer time at the interface than in the case of the wider viscosity gradient.

B. Case II: Tail-first, positive viscosity gradient

In this second case, the same swimmer is also placed near the top of the tank but the tail is oriented towards the interface. By reversing the rotation direction, the swimmer is then made to move

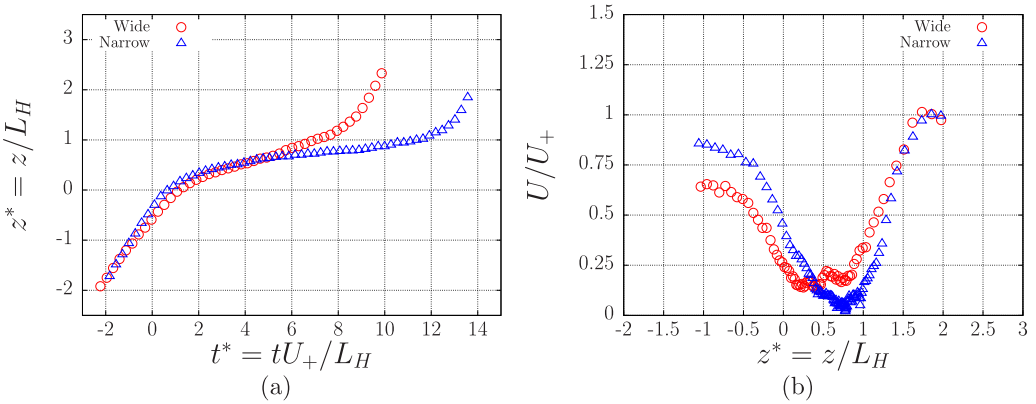

FIG. 5. Case I dynamics, head-first (pusher) swimmer crossing a positive viscosity gradient: (a) dimensionless position, z^*, as function of dimensionless time, t^*; (b) normalized speed U/U_+ as a function of dimensionless position z^*. At $t^* \approx 0$ the swimmer reaches the interface, located at $z^* \approx 0$.

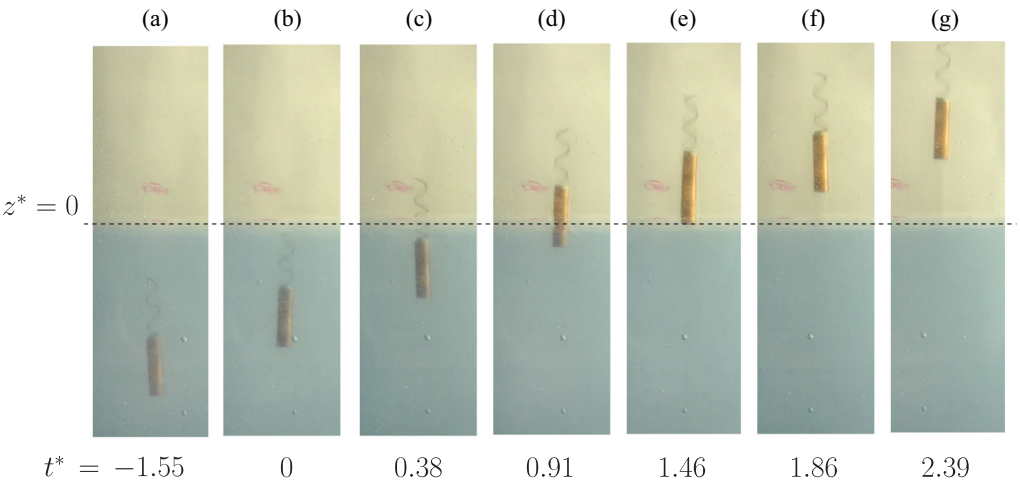

FIG. 6. Case II: time sequence of the tail-first (puller) swimmer crossing a positive viscosity gradient, for $\delta = 0.274$ (narrow gradient). Images have been flipped so that the swimmer appears to move upwards.

tail-first (puller mode). In Fig. 6 we show an image sequence of the process. The corresponding position and speed of the swimmer are plotted in Fig. 7.

As in the previous case, initially the swimmer moves at a constant speed when it is relatively far from the interface, see Fig. 6(a). In contrast with the previous case, when the tail of the swimmer reaches the interface, the swimming speed increases sharply [Fig. 6(b)]. The swimming speed continues to increase until the head reaches the interface [Fig. 6(c)]. The maximum speed reached is nearly twice that of the steady speed in the more viscous fluid. As the process progresses, the head crosses the interface and the swimming speed decreases from the maximum value to the free swimming value; see Fig. 6(f). The process can be observed clearly in the two plots that show normalized position and speed in Fig. 7. As in the previous case, the thickness of the viscosity gradient does not significantly change the process.

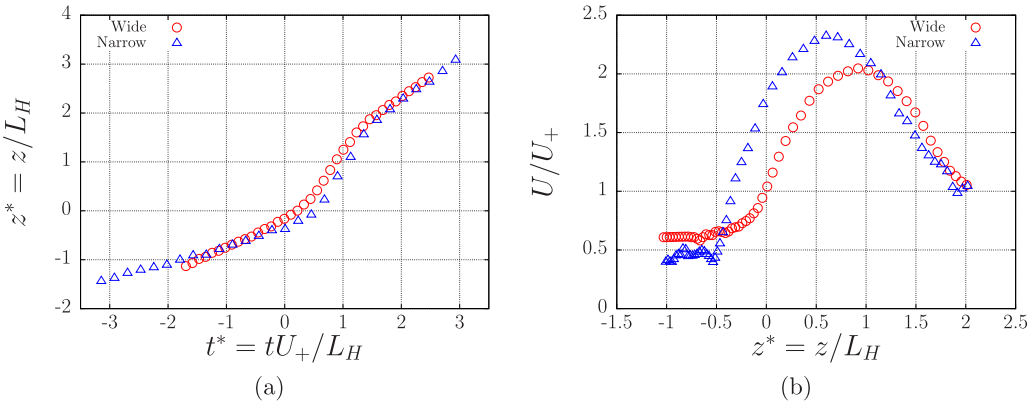

FIG. 7. Case II dynamics, tail-first (puller) swimmer crossing a positive viscosity gradient: (a) dimensionless position, z^*, as function of dimensionless time, t^*; (b) normalized speed U/U_+ as a function of dimensionless position z^*. At $t^* \approx 0$ the swimmer reaches the interface, located at $z^* \approx 0$.

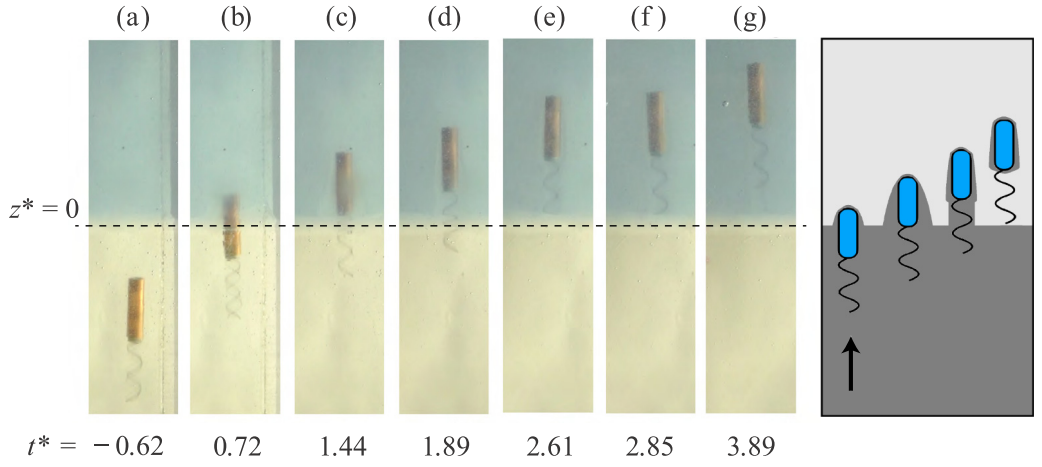

FIG. 8. Case III: time sequence of the head-first (pusher) swimmer crossing a negative viscosity gradient, for $\delta = 0.274$ (narrow gradient). The sketch on the right depicts the crossing dynamics schematically.

C. Case III: Head-first, negative viscosity gradient

In this third set of experiments, the swimmer moves up from the bottom of the tank head-first (i.e., in pusher mode) across a negative viscosity gradient. Interestingly, we find some important differences with case I. In Fig. 8 we show snapshots of the crossing process at different times while we plot in Fig. 9 the normalized position and the speed of the swimmer.

The experiment starts with the swimmer moving in the high-viscosity fluid at constant speed, $U_0^{\mu_+} = U_+ = 3.2$ mm/s; see Fig. 8(a). As in the previous cases, the swimmer slows as it approaches the interface, but the process is different from case I since, although in both cases the swimmer approaches the interface head-first, the viscosity gradients are in opposite directions. In the case of a negative viscosity gradient, the swimmer appears to entrain some of the fluid with it as it crosses the interface, as can be seen in Figs. 8(b) and 8(c). This results in the swimming speed staying relatively constant during the crossing of the head. Once the head of the swimmer has completely crossed the interface, the tail remains in the more viscous fluid [Fig. 8(d)] and the speed decreases

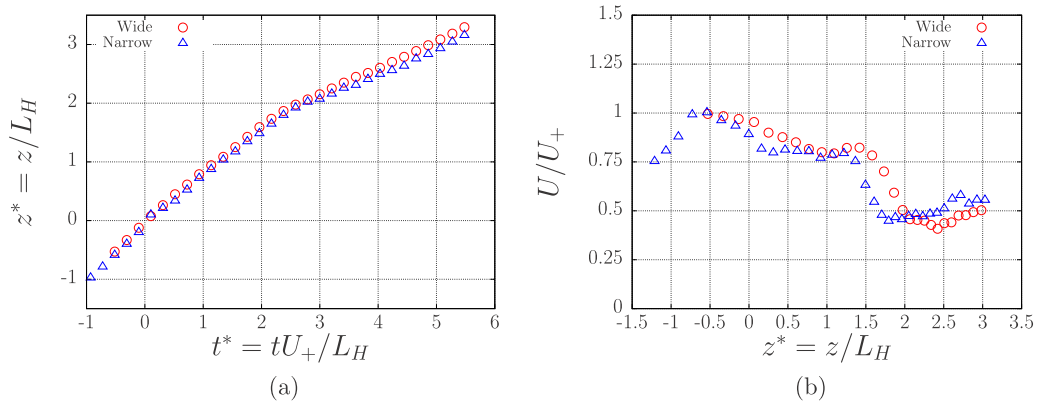

FIG. 9. Case III dynamics, head-first swimmer (pusher) crossing a negative viscosity gradient: (a) dimensionless position, z^*, as function of dimensionless time, t^*; (b) normalized speed U/U_+ as a function of dimensionless position z^*. At $t^* \approx 0$ the swimmer reaches the interface, located at $z^* \approx 0$.

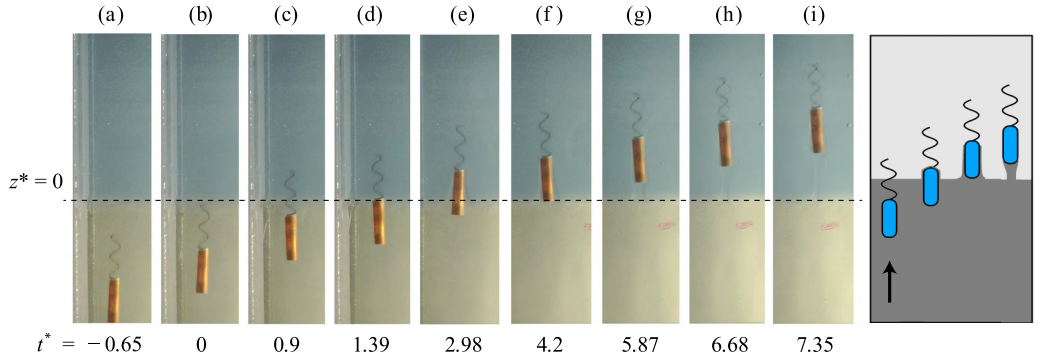

FIG. 10. Case IV: Time sequence of the tail-first swimmer crossing the viscosity gradients from high to low viscosity. The sketch on the right shows the crossing dynamics schematically.

sharply. At later times, the speed of the swimmer slowly increases until it reaches the free swimming speed $U_0^{\mu-}$; see Figs. 8(f) and 8(g). We note that the thickness of the viscosity gradient does not seem to affect the crossing process significantly.

D. Case IV: Tail-first, negative viscosity gradient

The final case considers the dynamics of the swimmer moving tail-first from the high to low viscous fluid (negative gradient). In case II, when the swimmer also moved tail-first, a significant increase of the swimming speed was observed during the interface crossing process. As shown below, the behavior in this case is quite different.

In this case, the swimmer moves upwards from the bottom of the tank, approaching the interface tail-forward. A sequence of images of the dynamics are shown in Fig. 10, and we display in Fig. 11 the corresponding position and speed of the swimmer for the two experiments with narrow and wide viscosity gradients (as in all previous cases, Fig. 10 illustrates only the motion in the case of a narrow viscosity gradient).

The swimmer starts to move from the bottom of the tank towards the viscosity interface at a constant speed; see Fig. 10(a). When the tail reaches the viscosity interface, the speed increases slightly [Fig. 10(b)] but then continuously decreases as the swimmer crosses the interface [see

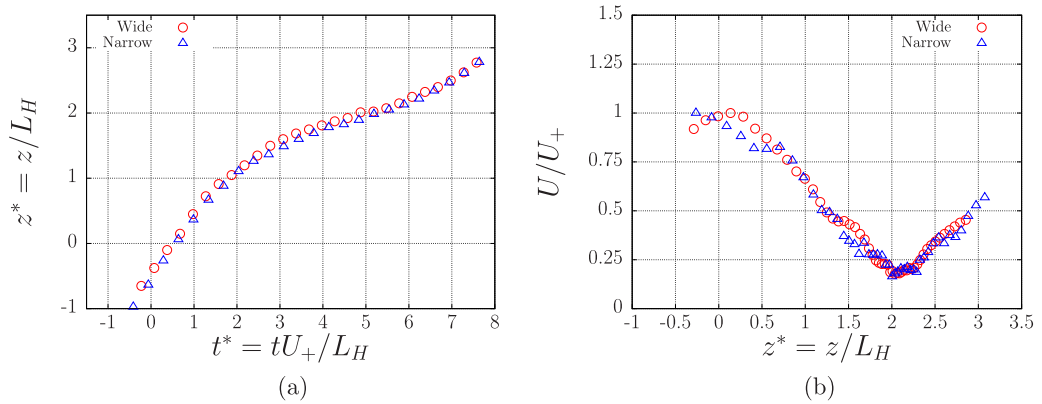

FIG. 11. Case IV dynamics, tail-first (puller) swimming crossing negative viscosity gradient: (a) dimensionless position, z^*, as function of dimensionless time, t^*; (b) normalized speed U/U_+ as a function of dimensionless position z^*. At $t^* \approx 0$ the swimmer reaches the interface, located at $z^* \approx 0$.

Figs. 10(c)–10(f)], reaching a minimum speed when the head finally reaches $z^* \approx 0$. As in the previous case, as the swimmer crosses the gradient it is seen to entrain some of the more viscous fluid. The speed of the swimmer increases finally reaching its steady speed for $z^* > 3$ [see Figs. 10(h) and 10(i)], while the more viscous fluid entrained by the swimmer progressively returns to its location at the bottom of the tank.

IV. DISCRETE INTERFACE MODEL

As shown in the four cases studied experimentally above, a rich dynamical process is observed, resulting from the intricate balance between drag and thrust for a swimmer straddling two domains of different viscosities. Since the two-fluid arrangement is naturally stratified (the more-viscous fluid is denser), buoyancy may also play an important role in the process. Based on these observations, we now propose a model to describe the motion of a swimmer immersed in a fluid of nonhomogeneous viscosity. Following the experimental setup, the rigid swimmer consists of a cylindrical head and a helical tail. It rotates at a fixed angular speed $\mathbf{\Omega}$, causing the tail to rotate and push on the surrounding fluid, thus propelling the swimmer forward with velocity $\mathbf{U}$. The size of the swimmer, velocity of motion, and the viscosity of the fluid media are such that inertia can be neglected and we are in the creeping flow conditions. Assuming that the classical resistive-force theory of slender filaments [60] remains applicable locally at each point along the swimmer, the force per unit length acting on the swimmer is given by

$$\mathbf{f} = -\zeta_\perp \mathbf{u} + (\zeta_\perp - \zeta_\parallel)(\mathbf{u} \cdot \boldsymbol{\tau})\boldsymbol{\tau}, \tag{3}$$

where $\zeta_\perp$ and $\zeta_\parallel$ are, respectively, the perpendicular and parallel drag coefficients per unit length given by [61]

$$\zeta_\parallel^{H,T} \approx \frac{2\pi\mu}{\ln\left(L_{H,T}/r_{H,T}\right)}, \tag{4}$$

where the superscripts denote head (H) and tail (T). We also ignore hydrodynamic interactions between the tail and the head, an assumption that we can check *a posteriori* to be reasonable given the comparison between the model and the experimental results.

Using force balance we can then relate the swimming velocity to the angular velocity with a linear relationship, $\mathbf{U} = S\mathbf{\Omega}$, with a prefactor S that can be determined for different viscosity profiles. We start below with a sharp (step) function, which is a good approximation to a mixture of two miscible fluids of different viscosities at early times. We will next generalize to a continuous profile. We then complete the model by adding the effect of gravity to our calculations. The predictions of the model are finally compared against experimental data.

A. Sharp viscosity gradient

We start by analyzing the motion at early times when the gradient in viscosity is sharp. In this case we can model the fluid as two semi-infinite domains with viscosity

$$\mu(z) = \begin{cases} \mu_1 = \mu' & z \leqslant 0 \\ \mu_2 = \mu & 0 \leqslant z \end{cases}, \tag{5}$$

where $z = 0$ denotes the location of the interface (see Fig. 12). The analysis below will be valid for any viscosity distribution and any orientation. Indeed, if we express the swimming speed as a function of the distance from the head to the fluid interface, instead of the vertical coordinate z, we can describe the dynamics in cases I and III (head-first negative and positive gradient) by taking

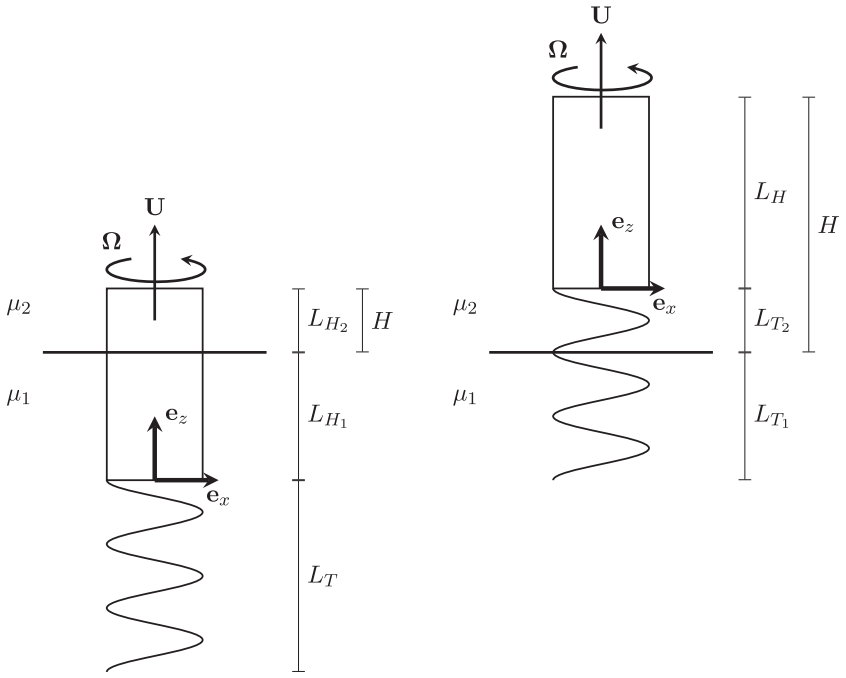

FIG. 12. Helical swimmer crossing a sharp viscosity gradient.

$\mu' < \mu$ and $\mu < \mu'$, respectively. As discussed in Sec. V A, the tail-first dynamics then follows from the reversibility of Stokes flow.

B. Head-first interaction

1. Head crossing

When the head crosses the viscosity gradient first (Fig. 12, left), we model the drag exerted on each part of the head as that experienced in an infinite fluid of viscosity $\mu_1 = \mu'$ or $\mu_2 = \mu$. The total viscous drag on the head is therefore given by

$$\mathbf{F}_D = -\left[\zeta^H_{\parallel_1} L_{H_1} + \zeta^H_{\parallel_2} L_{H_2}\right] U \mathbf{e}_z = -\zeta^H_{\parallel_1}\left[L_{H_1} + \frac{\mu_2}{\mu_1} L_{H_2}\right] U \mathbf{e}_z, \tag{6}$$

where $L_{H_{1,2}}$ are the lengths of the portions of the head above and below the interface (which therefore change in time as the swimmer moves through the interface). The resistance coefficients $\zeta^H_{\parallel_{1,2}}$ are proportional to the corresponding local viscosities and depend on the geometry of the head [62]. The tail is modeled as a right-handed helix of radius R and pitch angle ψ. We parametrize it using the arc-length $s = R\varphi/\sin\psi$, where φ is the azimuthal coordinate. The position $\mathbf{x}(s,t)$ of a material point on the tail is therefore given by (see Fig. 12)

$$\mathbf{x}(s,t) = R\cos(2\pi s/\ell + \Omega t)\mathbf{e}_x + R\sin(2\pi s/\ell + \Omega t)\mathbf{e}_y + (Ut + bs)\mathbf{e}_z, \tag{7}$$

where $\ell = 2\pi R/\sin\psi$ is the arc-length per helical turn and $b = \cos\psi$. The tangent ($\boldsymbol{\tau}$) and velocity vectors ($\mathbf{u}$) are obtained by differentiation with respect to s and t, respectively:

$$\boldsymbol{\tau}(s) = -\sin\psi\sin(2\pi s/\ell + \Omega t)\mathbf{e}_x + \sin\psi\cos(2\pi s/\ell + \Omega t)\mathbf{e}_y + \cos\psi\mathbf{e}_z, \tag{8}$$

$$\mathbf{u}(s) = -R\Omega\sin(2\pi s/\ell + \Omega t)\mathbf{e}_x + R\Omega\cos(2\pi s/\ell + \Omega t)\mathbf{e}_y + U\mathbf{e}_z. \tag{9}$$

The total hydrodynamic force exerted on the helix is then obtained using resistive-force theory as

$$\begin{aligned}\mathbf{F}_p &= -\int_0^{L_T/\cos\psi} \zeta_{\perp_1}^T \mathbf{u} + (\zeta_{\parallel_1}^T - \zeta_{\perp_1}^T)(\mathbf{u}\cdot\boldsymbol{\tau})\boldsymbol{\tau}\, ds \\ &= -\zeta_{\perp_1}^T \int_0^{L_T/\cos\psi} \mathbf{u} + (\beta^T - 1)(\mathbf{u}\cdot\boldsymbol{\tau})\boldsymbol{\tau}\, ds, \end{aligned} \tag{10}$$

where $\zeta_{\perp_1}^T$, $\zeta_{\parallel_1}^T$ are the perpendicular and parallel drag coefficients for the helix center line filament and $\beta^T = \zeta_{\parallel_1}^T/\zeta_{\perp_1}^T$, approximately equal to $1/2$ in the slender limit [60]. Ignoring end effects, the propulsive force acts mainly in the z direction, therefore we evaluate

$$\begin{aligned}\mathbf{e}_z\cdot\mathbf{F}_p &= -\zeta_{\perp_1}^T \int_0^{L_T/\cos\psi} [U + (\beta^T - 1)b(\Omega R\sin\psi + Ub)]\, ds \\ &= -\frac{\zeta_{\perp_1}^T L_T}{\cos\psi}\{U[1 + (\beta^T - 1)\cos^2\psi] + (\beta^T - 1)\Omega R\sin\psi\cos\psi\}. \end{aligned} \tag{11}$$

We obtain the swimming velocity in terms of the angular velocity by imposing the free swimming condition $\mathbf{e}_z\cdot(\mathbf{F}_p + \mathbf{F}_D) = 0$. The swimming speed is then given by

$$U = \frac{\zeta_{\perp_1}^T L_T(1-\beta^T)R\sin\psi\cos\psi\,\Omega}{\zeta_{\parallel_1}^H\cos\psi\left(L_{H_1} + \frac{\mu_2}{\mu_1}L_{H_2}\right) + \zeta_{\perp_1}^T L_T[1 + (\beta^T - 1)\cos^2\psi]}. \tag{12}$$

Using the condition $L_{H_1} + L_{H_2} = L_H$ and defining $\lambda \equiv L_T/L_H$, $\xi \equiv \zeta_{\perp_1}^T/\zeta_{\parallel_1}^H$ and $\ell_H \equiv L_{H_2}/L_H$, we can write the swimming speed as a function of $\ell_H = h$ as

$$U_1(h) = \frac{\xi\lambda(1-\beta^T)R\sin\psi\cos\psi\,\Omega}{\cos\psi\left(1 + \frac{\mu_2-\mu_1}{\mu_1}h\right) + \xi\lambda[1 + (\beta^T - 1)\cos^2\psi]}, \tag{13}$$

where $h \equiv H/L_H$ is the dimensionless position of the swimmer's head.

2. Tail crossing

After the head has crossed the interface completely ($h = 1$) the force balance changes. In this case, the head is completely immersed in the fluid of viscosity μ_2, and the drag on the head is given by

$$\mathbf{F}_D = -\zeta_{\parallel_2}^H L_H U\mathbf{e}_z. \tag{14}$$

On the other hand, the propulsive force from the tail as it crosses the interface (Fig. 12, right) is now given by

$$\mathbf{e}_z\cdot\mathbf{F}_p = -\frac{\zeta_{\perp_1}^T L_{T_1} + \zeta_{\perp_2}^T L_{T_2}}{\cos\psi}\{U[1 + (\beta^T - 1)\cos^2\psi] + (\beta^T - 1)\Omega R\sin\psi\cos\psi\}, \tag{15}$$

where β^T is independent of the viscosities. Applying the free swimming condition along z, we then obtain the swimming speed

$$U = \frac{\xi\lambda\left(\frac{\mu_2}{\mu_1} + \frac{\mu_1-\mu_2}{\mu_1}\ell_T\right)(1-\beta^T)R\sin\psi\cos\psi\,\Omega}{\cos\psi\frac{\mu_2}{\mu_1} + \xi\lambda\left(\frac{\mu_2}{\mu_1} + \frac{\mu_1-\mu_2}{\mu_1}\ell_T\right)[1 + (\beta^T - 1)\cos^2\psi]}, \tag{16}$$

where we have used the fact that $\zeta_{\perp_2}^T/\zeta_{\parallel_2}^H = \zeta_{\perp_1}^T/\zeta_{\parallel_1}^H = \xi$ and defined $\ell_T \equiv L_{T_1}/L_T$. The position of the top part of the head is now $H = L_H[1 + \lambda(1 - \ell_T)]$, so we can rewrite Eq. (16) in terms of h as follows:

$$U_2(h) = \frac{\xi\left[\lambda + \frac{\mu_2-\mu_1}{\mu_1}(h-1)\right](1-\beta^T)R\sin\psi\cos\psi\,\Omega}{\cos\psi\frac{\mu_2}{\mu_1} + \xi\left[\lambda + \frac{\mu_2-\mu_1}{\mu_1}(h-1)\right][1 + (\beta^T - 1)\cos^2\psi]}. \tag{17}$$

3. Summary

In the calculations above we obtained that $U_1(\ell_H = 0) = U_2(\ell_T = 0) = U_0$, so the swimming speeds are identical when the swimmer is completely immersed in either of the two fluids. The final speed of the swimmer is then given parametrically by

$$U(h) = \begin{cases} U_0 & h < 0, \\ U_1(h) & 0 \leqslant h \leqslant 1, \\ U_2(h) & 1 < h < 1 + \lambda, \\ U_0 & 1 + \lambda < h. \end{cases} \tag{18}$$

We further note that the information about the direction of motion is only embedded in the values of the viscosities, hence Eq. (18) is the swimming speed in case I when $\mu_1 = \mu' < \mu_2 = \mu$, and case III for the choice $\mu < \mu'$.

C. Swimmer position

When the head crosses the interface, the swimming speed is of the form

$$U_1(h) = \frac{A_1}{B_1 + C_1 h}\Omega, \tag{19}$$

where

$$A_1 = \xi\lambda(1 - \beta^T)R \sin\psi\cos\psi, \tag{20}$$

$$B_1 = \cos\psi + \xi\lambda[1 + (\beta^T - 1)\cos^2\psi], \tag{21}$$

$$C_1 = \frac{\mu_2 - \mu_1}{\mu_1}\cos\psi. \tag{22}$$

On the other hand, when the tail crosses the interface, the speed is of the form

$$U_2(h) = \frac{A_2 + D_2 h}{B_2 + C_2 h}\Omega, \tag{23}$$

where

$$A_2 = \xi\lambda'(1 - \beta^T)R \sin\psi\cos\psi, \tag{24}$$

$$D_2 = \xi\frac{\mu_2 - \mu_1}{\mu_1}(1 - \beta^T)R \sin\psi\cos\psi, \tag{25}$$

$$B_2 = \cos\psi\frac{\mu_2}{\mu_1} + \xi\lambda'[1 + (\beta^T - 1)\cos^2\psi], \tag{26}$$

$$C_2 = \xi\frac{\mu_2 - \mu_1}{\mu_1}[1 + (\beta^T - 1)\cos^2\psi], \tag{27}$$

where $\lambda' = \lambda - (\mu_2 - \mu_1)/\mu_1$.

The swimming speed is the derivative with respect to time of the position of the head, therefore to find the position we need to integrate the ordinary differential equation

$$L_H\frac{dh_i}{dt} = U_i(h). \tag{28}$$

That equation is separable and can be integrated to obtain $h_1(t)$ and $h_2(t)$ as solutions of

$$B_1 h_1 + C_1\frac{h_1^2}{2} = \frac{A_1}{L_H}\Omega t, \tag{29}$$

$$L_H\left[\frac{D_2B_2 - A_2C_2}{D_2^2}\ln\left(\frac{A_2 + D_2h_2}{A_2 + D_2}\right) + \frac{C_2}{D_2}(h_2 - 1)\right] = \Omega(t - T_1), \tag{30}$$

where $T_1 = L_H(2B_1 + C_1)/(2A_1\Omega)$ satisfies $h(T_1) = 1$, that is, T_1 is the time at which the head has fully crossed the interface. Taking the condition $h(0) = 0$, we then choose the positive branch of Eq. (29) so the position of the head for $0 \leqslant t \leqslant T_1$ is given by

$$h_1 = \frac{B_1}{C_1}\left[\left(1 + 2\frac{A_1 C_1 \Omega t}{L_H B_1^2}\right)^{1/2} - 1\right]. \tag{31}$$

In the second period, $T_1 \leqslant t \leqslant T_2$, the position of the head is given implicitly as the solution of

$$\cos\psi \ln\left[1 + \frac{\mu_2 - \mu_1}{\lambda\mu_1}(h_2 - 1)\right] + C_2(h_2 - 1) = \frac{D_2}{L_H}\Omega(t - T_1), \tag{32}$$

where we used Eqs. (24)–(27) while $T_2 = L_H[\cos\psi \ln(\mu_2/\mu_1) + C_2\lambda]/(D_2\Omega) + T_1$ is the time at which the tail has completely crossed the interface, the solution to $h_2(T_2) = 1 + \lambda$. As the swimming speed is constant, $U = U_0$, for $h \leqslant 0$ and $1 + \lambda \leqslant h$, or equivalently $t \leqslant 0$ and $T_2 \leqslant t$, the position of the head as a function of time is given by

$$h(t) = \begin{cases} U_0 t & t \leqslant 0, \\ h_1(t) & 0 \leqslant t \leqslant T_1, \\ h_2(t) & T_1 \leqslant t \leqslant T_2, \\ 1 + \lambda + U_0(t - T_2) & T_2 \leqslant t. \end{cases} \tag{33}$$

D. Buoyancy

In order to maintain a stable two-fluid configuration, the fluids must have different densities. Experimentally, salt was added to the high-viscosity fluid to slightly increase its density. The effect on the swimmer is to add a buoyancy term in the force balance equation $(\mathbf{F}_D + \mathbf{F}_p + \mathbf{F}_g) \cdot \mathbf{e}_z = 0$, where the buoyancy term is given by

$$\mathbf{F}_{g1} = \left\{\pi R^2[L_{H_1}(\rho_H - \rho_1) + L_{H_2}(\rho_H - \rho_2)] + \pi a^2 \frac{L_T}{\cos\psi}(\rho_T - \rho_1)\right\}\mathbf{g}, \tag{34}$$

for $0 \leqslant h \leqslant 1$ and

$$\mathbf{F}_{g2} = \left\{\pi R^2 L_H(\rho_H - \rho_2) + \frac{\pi a^2}{\cos\psi}[L_{T_1}(\rho_T - \rho_1) + L_{T_2}(\rho_T - \rho_2)]\right\}\mathbf{g}, \tag{35}$$

for $1 \leqslant h \leqslant 1 + \lambda$. Here ρ_H and ρ_T are the effective densities of the head and the helical tail respectively, the density of fluid $i = 1, 2$ is denoted by ρ_i and $\mathbf{g}$ is the gravitational acceleration. As none of these expressions contain the swimming speed U explicitly, we can modify Eq. (13) and Eq. (17) to include an extra buoyancy term U_{gi} on the right-hand side, given by

$$U_{g1} = \frac{(\mathbf{F}_{g1} \cdot \mathbf{e}_z)\cos\psi}{\zeta^H_{\parallel_1}\cos\psi\left(L_{H_1} + \frac{\mu_2}{\mu_1}L_{H_2}\right) + \zeta^T_{\perp_1} L_T[1 + (\beta^T - 1)\cos^2\psi]}, \tag{36}$$

$$U_{g2} = \frac{\mathbf{F}_{g2} \cdot \mathbf{e}_z \cos\psi}{\zeta^H_{\parallel_2}\cos\psi L_H + \left(\zeta^T_{\perp_1} L_{T_1} + \zeta^T_{\perp_1} L_{T_2}\right)[1 + (\beta^T - 1)\cos^2\psi]}. \tag{37}$$

Defining the typical buoyancy speed $u^H_{gi} \equiv \pi R^2(\rho_H - \rho_i)\mathbf{g} \cdot \mathbf{e}_z/\zeta^H_{\parallel_i}$ we can then write

$$U_{g1} = \frac{u^H_{g1}}{B_1 + C_1 h}\left[\left(1 + \frac{\rho_1 - \rho_2}{\rho_H - \rho_1}h\right)\cos\psi + \lambda\frac{a^2}{R^2}\frac{\rho_T - \rho_1}{\rho_H - \rho_1}\right], \tag{38}$$

$$U_{g2} = \frac{u^H_{g2}}{B_2 + C_2 h}\left[\cos\psi + (h - 1)\frac{a^2}{R^2}\frac{\rho_1 - \rho_2}{\rho_H - \rho_2} + \lambda\frac{a^2}{R^2}\frac{\rho_T - \rho_1}{\rho_H - \rho_2}\right], \tag{39}$$

where B_i and C_i are as given in Eqs. (21), (22), (26), and (27).

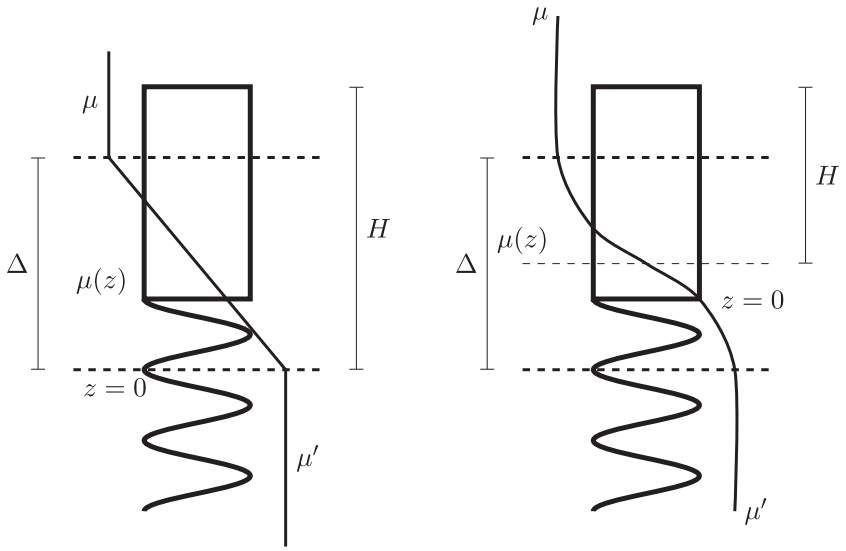

FIG. 13. Continuous viscosity gradient with a transition region of size Δ. Left: a linear viscosity profile between two fluid layers of viscosities μ' and μ. Right: a diffuse layer with $\Delta \sim \sqrt{Dt}$, where D is the diffusivity of $\mu(z)$.

V. CONTINUOUS INTERFACE MODEL

At short times after depositing the fluids in the tank, the interface between the two fluid mixture is sharp and the analysis of Sec. IV A is appropriate. At later times, however, the components responsible for the increase in the viscosity of the fluid mixture diffuse, and therefore so does the viscosity profile (see our measurements in Sec. II A). Therefore, we need to include in our calculations for the swimming speed, the case in which the viscosity distribution is continuous. We can achieve this by using a local drag coefficient $\zeta_{\perp,\parallel}^{H,T}(\mu(z))$ in the resistive force calculation above. Here $\mu(z)$ is the value of the local viscosity of the fluid at some point on the body of the swimmer at a distance z from the fluid interface. Considering a viscosity profile such that $\mu(z \to -\infty) \to \mu'$ and $\mu(z \to \infty) \to \mu$ (see Fig. 13), the drag, propulsion, and buoyancy forces are then given by the linear superposition

$$\mathbf{e}_z \cdot \mathbf{F}_D = -\int_{H-L_H}^{H} \zeta_{\parallel}^{H}(\mu(z))U\, dz = -\zeta_{\parallel}^{H}(\mu')L_H U \int_{h-1}^{h} \frac{\tilde{\mu}(z)}{\mu'}\, dz, \tag{40}$$

$$\begin{aligned}\mathbf{e}_z \cdot \mathbf{F}_p &= -\int_0^{L_T/\cos\psi} \zeta_{\perp}^{T}\{\mu[z(s)]\}\, ds\{U[1+(\beta^T-1)\cos^2\psi] + (\beta^T-1)\Omega R \sin\psi\cos\psi\} \\ &= -\frac{\zeta_{\perp}^{T}(\mu')L_H}{\cos\psi}\int_{h-1-\lambda}^{h-1} \frac{\tilde{\mu}(z)}{\mu'}\, dz\{U[1+(\beta^T-1)\cos^2\psi] + (\beta^T-1)\Omega R\sin\psi\cos\psi\},\end{aligned} \tag{41}$$

$$\mathbf{F}_g = \pi R^2 L_H\left\{\int_{h-1}^{h}[\rho_H - \tilde{\rho}(z)]\, dz + \frac{a^2}{R^2\cos\psi}\int_{h-1-\lambda}^{h-1}[\rho_T - \tilde{\rho}(z)]\, dz\right\}\mathbf{g}, \tag{42}$$

where $\tilde{\mu}(z) = \mu(L_H z)$, and $\tilde{\rho}(z) = \rho(L_H z)$ with $\rho(z)$ the continuous density distribution of the fluid along z. Applying the free-swimming condition $\mathbf{F}_D + \mathbf{F}_p + \mathbf{F}_g = 0$, and solving for U, we obtain

the swimming speed in the continuous case as

$$U(h) = \frac{\xi\left[\int_{h-1-\lambda}^{h-1} \frac{\mu(z)}{\mu'}\, dz\right](1-\beta^T)\sin\psi\cos\psi R\Omega + (\mathbf{F}_g \cdot \mathbf{e}_z \cos\psi/\zeta_\parallel^H L_H)}{\cos\psi\left[\int_{h-1}^{h} \frac{\mu(z)}{\mu'}\, dz\right] + \xi\left[\int_{h-1-\lambda}^{h-1} \frac{\mu(z)}{\mu'}\, dz\right][1+(\beta^T-1)\cos^2\psi]}. \tag{43}$$

Note that the transition between μ' and μ does not have to be monotonic. However, in order to apply this model to the experiments presented in Sec. III we will choose a monotonic viscosity profile, with a transition region $\delta \equiv \Delta/L_H$, such as the linear and diffuse distributions depicted in Fig. 13. Again, the dynamics in cases I and III are obtained by setting $\mu' < \mu$ and $\mu < \mu'$, respectively.

The position of the swimmer as a function of time $h(t)$ can then be obtained by solving the ordinary differential equation

$$L_H \frac{dh}{dt} = U(h). \tag{44}$$

This might not be solvable analytically for an arbitrary viscosity profile, but it is straightforward to do numerically. As a final remark, note that we can recover the swimming speed in the two-fluid case, by setting $\tilde{\mu}(z<0) = \mu'$, $\tilde{\mu}(z>0) = \mu$ in Eq. (43). More generally, for any discrete number of fluid layers the swimming speed is found by replacing the integrals in Eq. (43) by the appropriate sums.

A. Head-first versus tail-first approach

The calculations above were all carried out in the case where the head of the swimmer crosses the interface first (pusher mode). Since the motion is dominated by viscosity, expressions for the speed when the swimmer approaches the interface with the tail first may then be obtained by time reversal. Indeed, time reversal of Stokes flow corresponds to the map $\{U, \Omega, h, \mu', \mu\} \mapsto \{-U, -\Omega, -h, \mu, \mu'\}$, therefore the tail-first approach is obtained by evaluating Eq. (43) at $h' = -h + \lambda + 1$, where the translation $\lambda + 1$ comes from the fact that $h' = 0$ corresponds to the moment when the tail meets the fluid interface. Note that we need to be careful with the sign of the gravitational field, and to remember that in the experiments, the high-viscosity fluid always sits at the bottom, so $\mathbf{F}_g \cdot \mathbf{e}_z < 0$ when the swimmer crosses from high to low viscosity and vice versa.

B. Model predictions: Parameter dependence

Before comparing the model predictions with the experimental data, we explore the impact of the different parameters of the problem on the swimming speed. One of the advantages of the model developed here is that it allows us to explore a wider set of conditions than those attainable experimentally. In this and the following section we will adopt the convention $\mu' < \mu$ for clarity. This means that, when the swimmer moves up the gradient, $\mu(h \to -\infty) \to \mu'$ and $\mu(h \to \infty) \to \mu$. When the swimmer moves down the gradient, we swap μ' and μ. Furthermore, we will use the terminology defined in Table I to refer to the different swimming conditions.

To simplify the interpretation of predictions, we first neglect buoyancy; in such a case, the time-reversal symmetry between the head-first and tail-first is exact. The dimensional parameters we are left with are the sizes of the swimmer (L_H, r_H, L_T, r_T) and the pitch of the helical tail (P_T). Another length scale is the size of the transition region (Δ) or, equivalently, the time at which the experiment is performed after the two-fluid mixture is set up. We will keep the proportions of the head fixed as well as the pitch and thickness of the helical filament so that we are left with two dimensionless parameters: $\delta = \Delta/L_H$ and $\lambda = L_h/L_H$, which quantify the relative size of the transition region and the size of the tail compared to the head of the swimmer. Finally, we will also consider variations in the viscosity ratio of the initial two-mixture fluid, i.e., μ/μ'.

In Fig. 14 we first show the swimming speed as a function of the distance between the head and the fluid-fluid interface (normalized by the initial, and terminal, speed U_0). We assume that

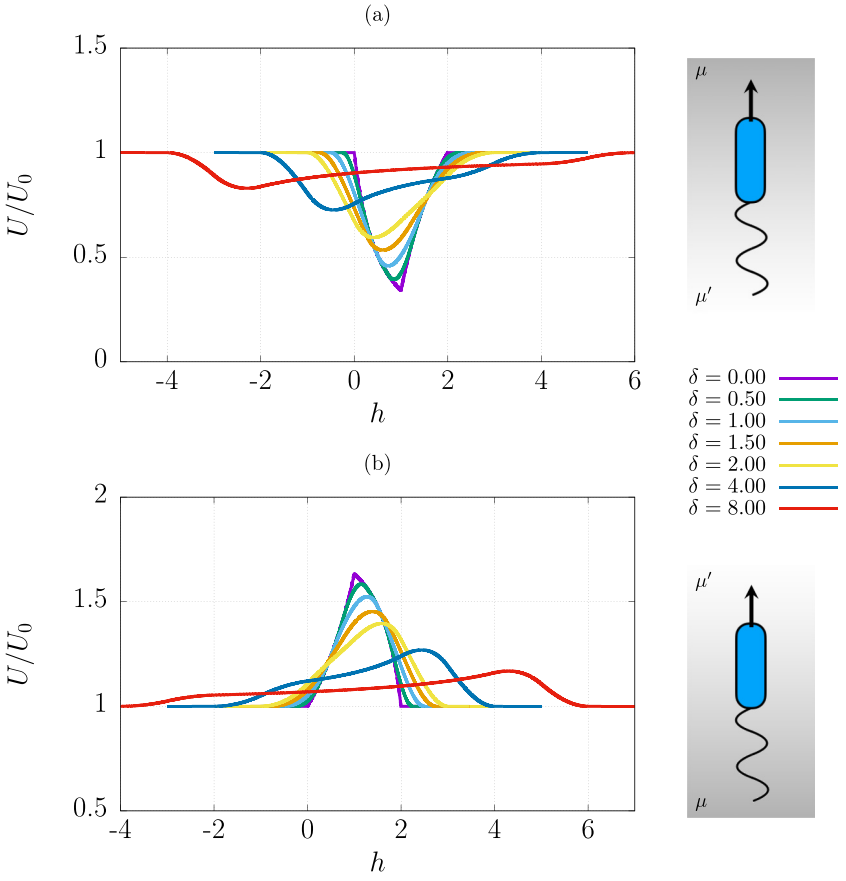

FIG. 14. Swimming speed in a linear viscosity gradient for different widths of the transition region. (a) Case I, (b) case III. The viscosities of the semi-infinite fluids on either side of the interface are given by the experimental values, i.e., $\mu' = \mu_- = 0.55\,\mathrm{Pa\,s}$ and $\mu = \mu_+ = 2.74\,\mathrm{Pa\,s}$. The length of the tail and head are the same, i.e., $\lambda = 1$, and the swimmer is neutrally buoyant in both fluids. The diagrams on the right indicate the direction of motion, with dark and light gray representing high (μ) and low viscosity (μ'), respectively. The values are normalized by the terminal speed U_0.

the viscosity varies linearly between the two experimental values, $\mu' = \mu_- = 0.55\,\mathrm{Pa\,s}$ and $\mu = \mu_+ = 2.74\,\mathrm{Pa\,s}$, and we take the head and tail to have the same lengths, i.e., $\lambda = 1$. In Fig. 14(a) we consider case I, and the fluid interface is located at $h = 0$. The speed is constant when the swimmer is completely immersed on the low-viscosity fluid. As the head crosses the interface, the drag increases but the propulsion stays the same, therefore the speed decreases. Once the tail meets the interface, the propulsion starts to increase thereby compensating the drag, and thus the speed increases until it plateaus back to a constant speed. Figure 14(b) shows the speed of the swimmer in case III. Here the drag reduces as the head traverses the interface, and hence the swimming speed increases until the tail meets the interface, when the propulsion starts decreasing, compensating for the lower drag. This continues until the swimmer is completely immersed in the top fluid, at which point the speed reaches a new constant value.

The speed of the swimmer in case II (tail-first) may be obtained by reflecting Fig. 14(b) on the vertical axis $h = 1$, with h now measured from the tip of the tail to the interface. Similarly for case IV, we reflect Fig. 14(a). Notice that for $\lambda = 1$, this reflection corresponds to the transformation $h \to -h + 1 + \lambda$. In general, for arbitrary λ, we need to reflect on the axis $h = (1 + \lambda)/2$ in order to

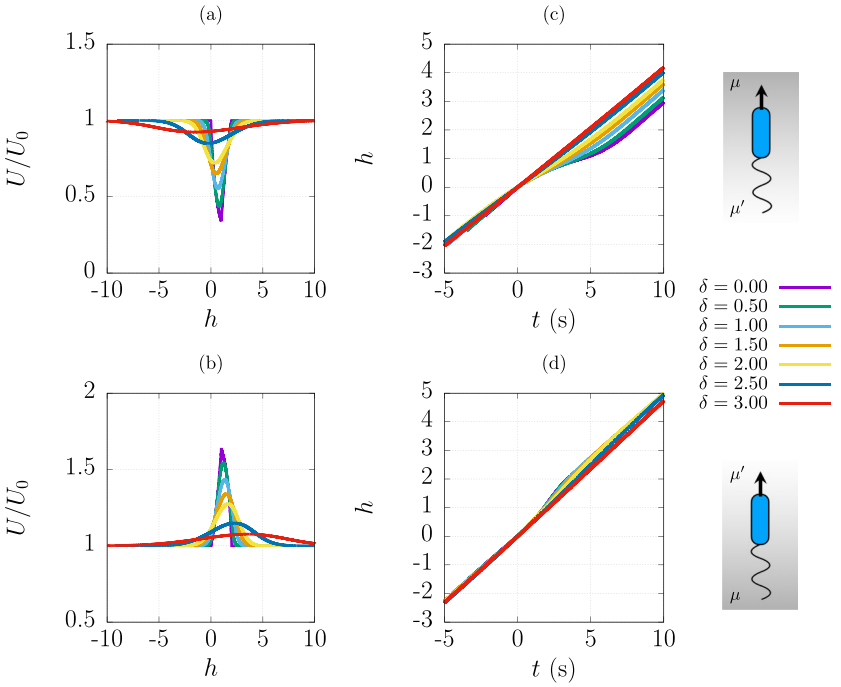

FIG. 15. Swimming speed in a diffusive viscosity gradient for different widths of the transition region. (a) Case I, (b) case III. The parameters $\{\mu/\mu', \lambda\}$ are the same as in Fig. 14.

obtain the swimming speed in the tail-forward scenarios. Therefore, the behavior of the swimming speed is reversed in the tail first approach: the swimming speed increases when it crosses from low to high viscosity and vice versa.

We next show in Figs. 15(a) and 15(b) analogous graphs to those in Fig. 14 for a diffusive viscosity gradient with different values of the transition length scale $\Delta = 2\sqrt{2Dt}$. The behavior is seen to be qualitatively the same as in the linear case. We also show the position of the swimmer as a function of time for the same conditions in Figs. 15(c) and 15(d). The evolution of the position is seen to not strongly depend on the width of the viscosity transition region, with the strongest variability occurring for case I [Fig. 15(c)].

The behavior of the swimmer dynamics with increasing values of the viscosity ratio (μ/μ') is shown in Fig. 16 (for values $\delta = 0.25$ and $\lambda = 1$). As could have been expected, the viscosity ratio greatly influences the amount by which the speed of the swimmer changes as it crosses the interface. In particular, when motion occurs from low to high viscosity, it is possible for the swimmer to spend an arbitrarily long time crossing the gradient if the viscosity ratio is large [see Figs. 16(a) and 16(c)]. In contrast, the effect on the dynamics when the swimmer crosses from high to low viscosity is less pronounced, with the time spent crossing the gradient decreasing by about 30% when the viscosity ratio is 1000 times larger.

The impact of the dimensionless length of the tail (λ) is next plotted in Fig. 17, for which we use the same size of the transition region and the viscosity values used in Fig. 14. The speed of the swimmer is seen to increase with the length of its tail, as expected since it is the tail that generates propulsion. We further observe that the time the swimmer takes to cross the interface decreases with λ in both cases.

We also observe that the speed changes less for swimmers with long tails; indeed, if the tail is much larger than the size of the transition region, then the propulsion remains almost the same during a crossing event. Therefore, we expect swimmers with short tails to be less efficient at crossing the interface.

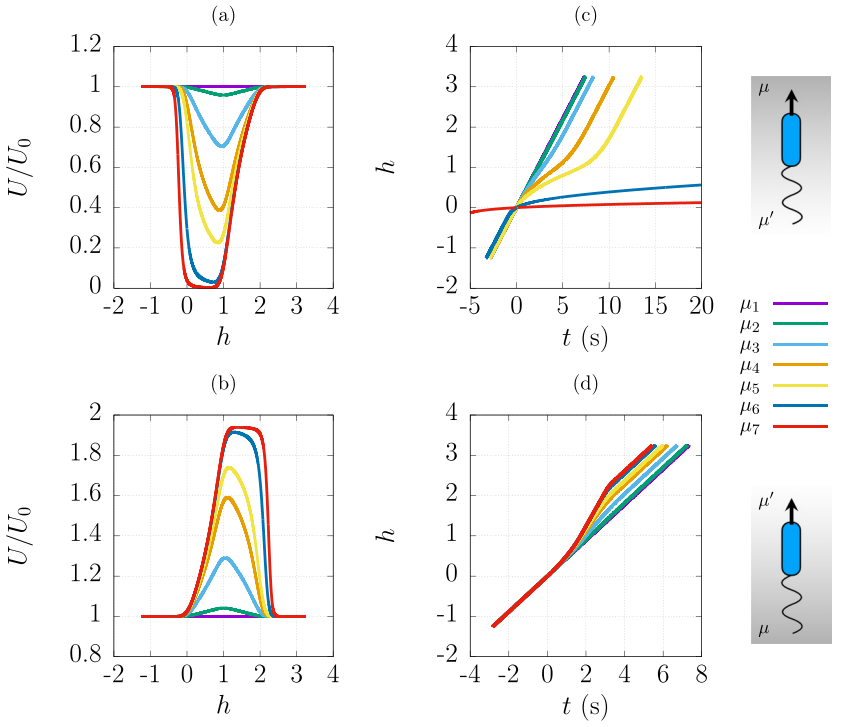

FIG. 16. Swimming speed and position in a diffusive viscosity gradient for different values of the viscosity ratio: $\mu_i/\mu' = 1.0$, 1.1, 2.0, 5.0, 10.0, 100.0, and 1000.0. (a), (c) Speed and position, Case I; (b), (d) speed and position, case III. The width of the transition region is $\delta = \Delta/L_H = 0.25$, the viscosity of the top fluid is $\mu' = \mu_- = 0.55\,\mathrm{Pa\,s}$ and $\lambda = 1$.

When buoyancy is considered, many additional parameters impact the penetration dynamics, in particular the relative densities between the swimmer's tail and head and the densities of the fluids. We did not explore all the dependencies, but it is important to point out two possible scenarios. In the situation where the bottom fluid is significantly denser than the top one, the swimmer could end up trapped at the interface between the two fluids in two different ways. Case (i) is the one where the head dominates the weight of the swimmer and case (ii) when the tail does. In case (i) the densities of the head and tail can be chosen in such a way that the propulsion is sufficiently large for the swimmer to cross the interface when moving head forwards down the viscosity gradient (assuming the bottom fluid is also the more viscous one), but then for the relative weight of the head in the top fluid to be so large that it opposes any further propulsion. Symmetrically, in case (ii), when the tail dominates the weight of the swimmer, it would be possible for the head of the swimmer, moving head first, to be light enough so as to provide buoyancy able to cancel the propulsion generated by the tail when the swimmer moves up the gradient. In both cases the swimmer would thus end up being trapped at the interface, like a buoy.

VI. COMPARISON WITH EXPERIMENTS

A. Positive viscosity gradient

In this section we compare the predictions of our model to the experiments of Sec. III.

We begin with the situation where the swimmer crosses the interface from the low- to the high-viscosity domain, and we start by analyzing case I, in which the head approaches the interface first. The swimmer moves at a constant speed when it is completely immersed in fluid 1. When the

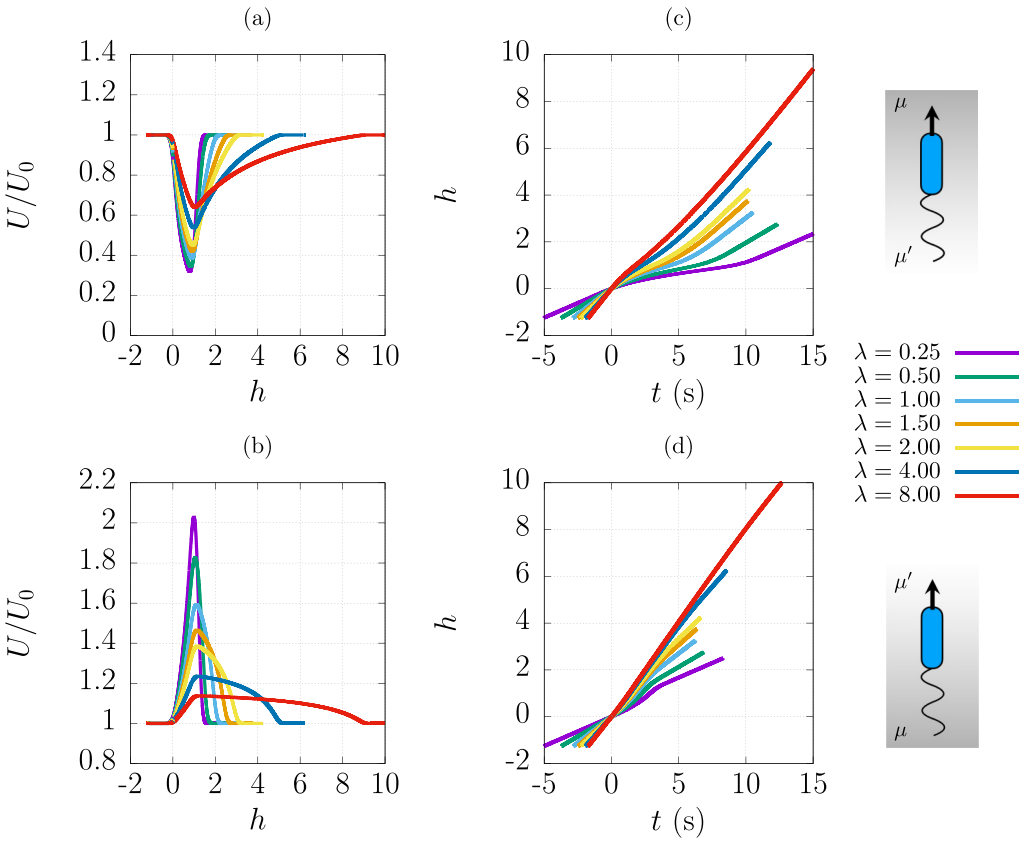

FIG. 17. Swimming speed and position in a diffusive viscosity gradient for different values of the tail-to-head size ratio, λ. (a), (c) Speed and position, case I; (b), (c) speed and position, case III. The width of the transition region is $\delta = \Delta/L_H = 0.25$, and the viscosity ratio is the same as in Fig. 14 (experimental values).

head reaches the interface, based on the results from the previous section, we expect the speed to decrease due to an increase in drag experienced by the head. When the tail meets the interface, the propulsion should then start to increase until it compensates the higher drag, achieving a constant terminal speed. Indeed, both Eq. (43) and the experimental data confirm this. We plot in Fig. 18 the speed of the swimmer (normalized by the swimming speed in the high-viscosity fluid) as a function of the dimensionless position of the head h; the swimmer starts from the low-viscosity fluid ($\mu' = \mu_- = 0.55$ Pa s) and approaches the interface head-first. We compare the experimental data against our model, Eq. (43), using the experimental parameters, i.e., $\lambda = 1$, $\mu = \mu_+ = 2.74$ Pa s, $\rho' = \rho_- = 1310$ kg/m^3, $\rho = \rho_+ = 1370$ kg/m^3 and an average density $\rho_{\text{swimmer}} = 1270$ kg/m^3 for the swimmer. The size of the transition region δ is obtained by the procedure described in Sec. II A. With no additional fitting parameters, we observe that our model matches the experiments very well, especially at early times [in the narrow viscosity gradient, indicated by (N)]. The model is able to predict also that the speed reduction decreases with an increase in the thickness of the fluid interface, δ.

Note that the swimming speed drops dramatically to less than 10% of its initial value when crossing the interface. This is a result of the combination of drag and buoyancy: as the swimmer crosses the interface, its velocity is reduced both by an increase in drag and by an increase in buoyancy (since the swimmer is slightly buoyant in both fluids; this is the least favorable case for it).

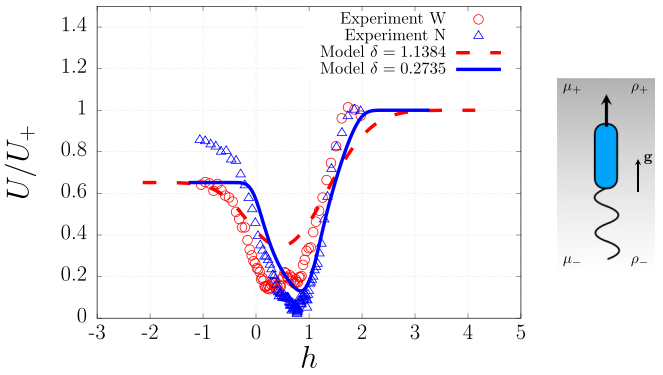

FIG. 18. Comparison between experiments and data for case I [i.e., head-first (pusher) swimmer crossing a positive viscosity gradient]: Speed of the swimmer as a function of the dimensionless position of the head h with respect to the interface located at $h = 0$. The speed is normalized by the speed in the fluid of high viscosity, $U_+ = U(h \to \infty)$. We display the measurements early after the viscosity gradient has been set up ([N]arrow gradient): triangles (experiment) and blue solid line (model), and 16 h after ([W]ide gradient): circles (experiment) and red dashed line (model).

In contrast to the head first approach, in case II (tail-first motion) we expect the swimmer to increase its speed as it traverses the viscosity gradient, this as a result of an increase in propulsion. When the head meets the interface, the drag increases and the speed should decrease, until the swimmer achieves a constant speed. Both our model in Eq. (43) and the experiments agree with this behavior, as shown in Fig. 19; we use the same values for the parameters λ and ρ_{swimmer} as in Figs. 18 and 20. The position h is now measured from the tip of the tail to the interface. We swap the values of the viscosities and densities $\mu' = \mu_+$, $\mu = \mu_-$, $\rho' = \rho_+$ and $\rho = \rho_-$, to be consistent with reversibility and the speed is still normalized by U_+. Here we also observe that the model can reproduce the experimental behavior, especially at early times. It can also capture the reduction of the increase in speed with the width of the transition region δ.

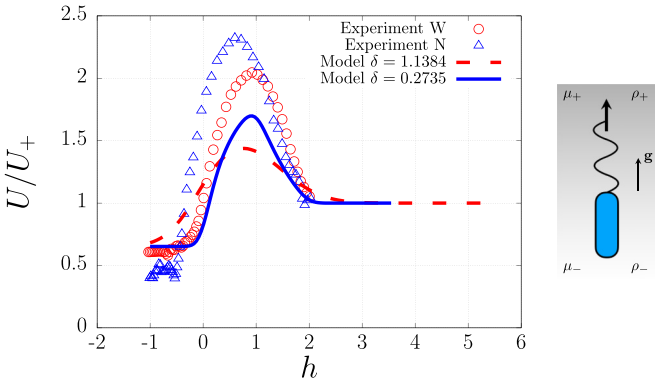

FIG. 19. Comparison between experiments and data for case II [tail-first (puller) swimmer in a positive viscosity gradient]. The speed of the swimmer is plotted as a function of the dimensionless position of the tail h with respect to the interface located at $h = 0$, and the speed is normalized by that in the high-viscosity fluid, $U_+ = U(h \to \infty)$. We show the measurements soon after the viscosity gradient has been set up ([N]arrow gradient case): triangles (experiment) and blue solid line (model), as well as 16 h after the start of the experiment ([W]ide gradient case): circles (experiment) and red dashed line (model).

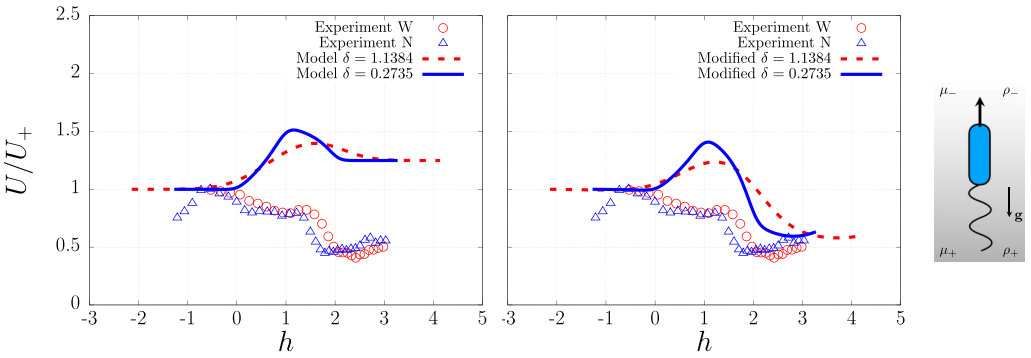

FIG. 20. Comparison between experiments and data for case III [i.e., head-first swimmer (pusher) crossing a negative viscosity gradient]. We plot the dimensionless speed of the swimmer as a function of the dimensionless position of the head h measured relative to the interface located at $h = 0$. The speed of the swimmer is normalized by the speed in the high-viscosity fluid, $U_+ = U(h \to -\infty)$. We display the measurements early after the viscosity gradient has been set up ([N]arrow gradient): triangles (experiment) and blue solid line (model), and 16 h after ([W]ide gradient): circles (experiment) and red dashed line (model). The figure on the left shows the predictions of the original model, not taking into account entrainment, while the plot on the right the modified model with variable buoyancy and $\alpha_{\max} = 0.1$.

B. Negative viscosity gradient

We now move on to the case where the swimmer crosses the interface from the high- to the low-viscosity region, that is swimming down the gradient. To compare the results against our model, Eq. (43), we use the same set of the parameters: $\mu' = \mu_+ = 2.74$ Pa s, $\mu = \mu_- = 0.55$ Pa s, $\rho' = \rho_+ = 1370$ kg/m^3, $\rho = \rho_- = 1310$ kg/m^3, $\rho_{\text{swimmer}} = 1270$ kg/m^3, and $\lambda = 1$. The width of the transition region, δ, is obtained as before by fitting Eq. (2) to the experimental data.

In case III (head-first) we expect to see a behavior opposite to that of case I. Again, the swimmer travels at constant speed when it is completely immersed in the high viscosity fluid. As predicted by our model, when the head crosses the interface we would expect the drag experienced by the swimmer to decrease, resulting in an increase in the swimming speed. Then, when the tail reaches the interface, the propulsion should decrease, compensating for the reduced drag, until the swimming speed reaches a constant value. However, the experimental data show a completely different behavior. We plot in Fig. 20 a comparison between the experimental data and the predictions of Eq. (43) (theoretical predictions are shown in thin lines). In the experiments, the swimmer seems to maintain a constant speed as the head crosses the interface. When the tail then meets the interface, the speed starts decreasing. It is only once the swimmer has fully crossed and is completely immersed in the low viscosity fluid that the speed starts to increase.

Based on experimental observations, we hypothesize that this counterintuitive behavior is due to the head of the swimmer entraining a significant amount of high-viscosity fluid with it as it crosses into the low-viscosity region, thereby increasing its effective density and being slowed down. We show experimental evidence of this entrainment in Fig. 21(a).

It is difficult to precisely calculate the amount of fluid that the swimmer entrains. However, we can use our model to show that an increase in the effective swimmer density leads to theoretical results closer to what is observed experimentally. In order to do that, we assume that the swimmer has an average density ρ_{swimmer} which increases by a height-dependent fraction $\alpha(h)$ as $[1 + \alpha(h)]\rho_{\text{swimmer}}$. The increase is set explicitly by the relation

$$\bar{\rho}(h) = [1 + \alpha(h)]\rho_{\text{swimmer}} = \frac{M_{\text{swimmer}} + M_f(h)}{V_{\text{swimmer}} + V_f(h)}, \tag{45}$$

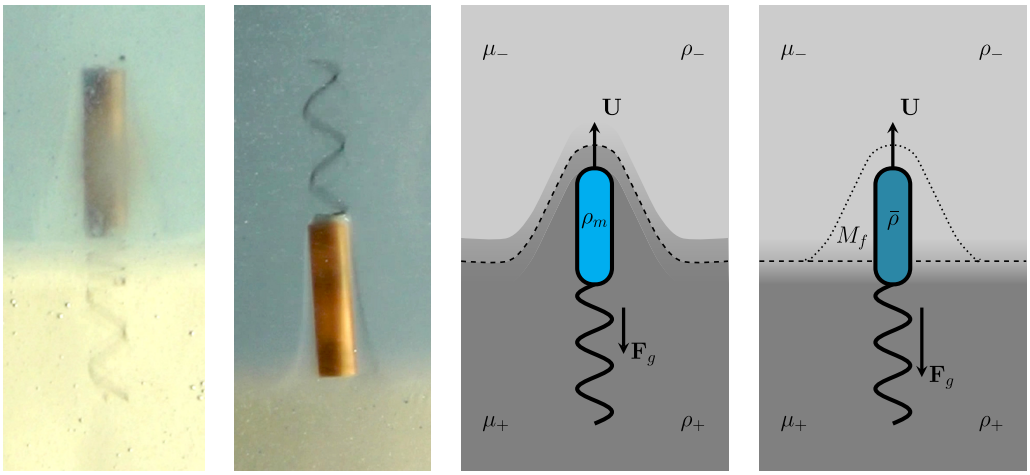

(a) (b)

FIG. 21. Viscous entrainment of the high-viscosity fluid by the swimmer. (a) Experimental picture showing the swimmer moving down the gradient and entraining some of the high-viscosity fluid as it crosses the interface, regardless of its orientation relative to the interface. (b) The entrained fluid accounts for an increase in the apparent density of the swimmer from $\rho_{\text{swimmer}} = M_{\text{swimmer}}/V_{\text{swimmer}}$ to $\bar{\rho} = [1 + \alpha(h)]\rho_{\text{swimmer}}$, where α depends on the mass of fluid dragged along with the swimmer, $M_f = \rho V_f$, as given in Eq. (45).

where $\{M_{\text{swimmer}}, V_{\text{swimmer}}\}$, $\{M_f, V_f\}$ are the masses and volumes of the swimmer and the entrained fluid, respectively [see Fig. 21(b)]. Therefore the maximum increase in density is obtained in the limit $1 \ll V_f/V_{\text{swimmer}}$ and is given by $\alpha_{\max} = (\rho_f - \rho_{\text{swimmer}})/\rho_{\text{swimmer}}$. Once the density reaches its maximum, the fluid slides off and the density decreases. This observation is consistent with previous calculations for the drift volume entrained by organisms in density stratified media [63]. At small Péclet number (i.e., for advection dominated by diffusion), the drift volume is a symmetric function of the distance to a reference line and it decreases as the swimmer moves away [63]. For finite Péclet number, the drift volume remains symmetric provided the Richardson number is small (i.e., for buoyancy negligible compared to viscous stresses). Here we assume that the shape remains symmetric, and we set α to be a Gaussian function with variance $[(1 + \lambda)/2 + \delta]^2$ and maximum $\alpha_{\max}$ at $h = 1 + \lambda + \delta$. This means that (1) the changes in apparent density are negligible before the swimmer meets the interface, (2) the maximum increase in density occurs when the swimmer has fully crossed the interface, and (3) most of the dragged fluid slides off after the swimmer has traveled the same distance it did before accumulating the maximum amount of entrained fluid.

Although this approach is a phenomenological way to account for the effect of the drift volume, it shows that an increase in the effective swimmer density plays an important role in the dynamics. We show in Fig. 20 the predictions of the modified model with the increase in density as thick lines. This new model is now able to capture the qualitative features observed in experiments.

We finally address the situation in case IV with a swimmer approaching the interface tail-first (puller case). Here we expect the swimming speed to slow as the swimmer crosses the gradient as a result of a decrease in propulsion. As soon as the head meets the interface the drag should decrease, compensating for the lower propulsion, until the speed reaches a constant value. However, we can see in Fig. 22 that in the experiments the swimmer does not increase its speed until it has completely crossed the viscosity gradient ($h = 0$), unlike the predictions from the original model (thin lines). An increase in the effective density of the swimmer due to entrainment of the high-viscosity fluid might here also be at the origin of this result. We use the modified model outlined above and plot its predictions in Fig. 22 as thick lines; we see that the new model is able to come closer to the

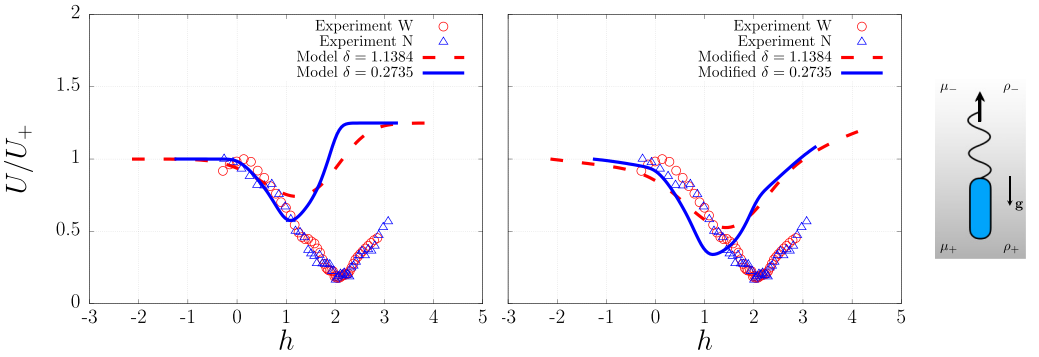

FIG. 22. Comparison between experiments and data for case IV (tail-first swimmer (puller) crossing the viscosity gradients from high to low viscosity): Speed of the swimmer as a function of the dimensionless position of the tail h with respect to the interface located at $h = 0$. Values for the speed are normalized by the speed in the high-viscosity fluid $U_+ = U(h \to -\infty)$. We display the measurements early after the viscosity gradient has been set up ([N]arrow gradient): triangles (experiment) and blue solid line (model), and 16 h after ([W]ide gradient): circles (experiment) and red dashed line (model). The figure on the left shows the predictions of the original model, while the plot on the right the modified model with variable buoyancy and $\alpha_{\max} = 0.1$.

experimental data. As for case II, here h is measured from the tip of the tail and we flip the values of the viscosities and densities to be consistent with reversibility, $\mu' = \mu_-$, $\mu = \mu_+$, $\rho' = \rho_-$, and $\rho = \rho_+$.

Since the viscosity of the bottom fluid is five times larger than that of the top fluid, the deformation of the interface and the amount of fluid that the swimmer carries with it are much smaller when it moves up the gradient (small entrainment of the low-viscosity fluid into the other one) than when it moves down the gradient (larger entrainment of the large-viscosity fluid). Therefore the correction to the buoyancy forces in cases I and II do not need to be included.

VII. CONCLUSION

In this paper, we present a joint experimental-theoretical study of the dynamics of synthetic magnetic helical swimmers moving across viscosity gradients between two miscible fluids. The viscosity gradients are seen to play a significant role in the swimming dynamics.

For motion up the viscosity gradient, there are two possible behaviors: first, for going up the gradient motion, if the swimmer moves head-first (pusher mode), its speed reduces due to an increase in drag. On the other hand, the swimmer increases its speed when it swims tail-first (puller mode), due to an increase in the viscous propulsion. When the swimmer moves instead from high- to low-viscosity regions, the opposite behavior is expected, i.e., the swimming speed should increase if the swimmer moves head-first and decrease if it moves tail-first. However, we observe in our experiments that the swimmer slows in both cases. We hypothesize that buoyancy forces resulting from entrainment of the high-viscosity fluid are responsible for such counterintuitive behavior: as the swimmer traverses the gradient, it drags a large amount of fluid with it, increasing its apparent mass and slowing its speed. We show evidence of this mechanism by modifying our model to include a buoyant term that increases as the swimmer advances. Although our model is able to capture many of the experimental features, its makes a number of simplifying assumptions (in particular hydrodynamic interactions between the head and the tail are neglected and drift is modeled in an *ad hoc* fashion). We believe that improvements are possible, and we hope to pursue them in future work.

Since we focus only on swimming motion parallel to the viscosity gradient in this paper, our model cannot tackle the issue of viscotaxis for single swimmers. However, our results suggest that,

regardless of the viscous entrainment, it is always harder for a pusher-like swimmer to swim up the gradient and that the opposite is true for a puller-like swimmer. Therefore, in addition to the reorientation of chiral swimmers in viscosity gradients [37], our results point to both positive and negative collective viscotaxis as being not only possible but governed solely by the motility pattern of the cells.

Specifically, let us consider microorganisms which perform a run-and-tumble dynamics, as is the case for many bacteria [64,65], and therefore swimmers that repeatedly stop their motion to change direction. For simplicity, we can assume that the swimmer's mode is always the same, i.e., that it always remains a puller or a pusher. For example *E. coli* remains a pusher during its swimming motion. If the motility pattern of the swimmer has a large positive directional persistence (i.e., the swimming direction after a reorientation event is close to the previous direction), then pusher-like swimmers would be predicted to statistically accumulate in regions of high viscosity (collective positive viscotaxis), because individual swimmers would spend more time in regions were they swim slower. The opposite situation would happen for puller-like swimmers (negative collective viscotaxis). In contrast, if the directional persistence is negative (i.e., reorientation angles larger than 90° on average), then pusher swimmers would exhibit negative collective viscotaxis while pullers would display positive viscotaxis.

The situation is more complex for bacteria such as *H. pylori* that can switch between swimming modes [66] or *V. alginolyticus* that exhibits a bimodal motility pattern with two different persistence parameters [64]. In the case of *H. pylori*, persistence is negative and the cell switches between pusher and puller modes during its locomotion. Using our results, we predict that a swimmer with this type of motility would accumulate in regions of high viscosity. This, in turn, would be advantageous for the cell as it would tend to spend longer times in the high-viscosity mucus layer that protects the stomach, ultimately leading to penetration and colonization of the stomach wall. On the other hand, our results also indicate that a healthy mucus layer will do its function if it remains narrow: if the bacteria remain at the viscosity gradient for too long, they would exhaust their available energy trying to cross the interface. The understanding of this process may be helpful in trying to understand prevention or remediation of gut infection and inflammation [67].

The reorientation towards, or away from, the gradient might of course modify the collective viscotactic effect. A recent theoretical study concluded that a squirmer swimming in a weak viscosity gradient will always reorient towards the direction of decreasing viscosity (negative viscotaxis), regardless of the swimming mode, puller or pusher [43]. This effect has been confirmed experimentally for the puller-like alga *C.reinhardtii* [68,69]. These studies showed that the green algae reorient against the viscosity gradient and perform collective negative viscotaxis. These results would seem to support our findings; however, *C.reinhardtii* swims at constant propulsive force rather than with a constant beating rate, and therefore its swimming speed decreases with increasing viscosity. At small viscosity ratios it is possible to observe a slight positive viscotactic effect, whereas for large viscosity ratios the viscous torque is strong enough for the cells to move away from high-viscosity regions. Another theoretical study found that positive viscotaxis is possible for a dumbbell swimmer which is driven by a force pulling on its leading pole, while negative viscotaxis happens for a dumbbell which is pushed on its back pole [37]. This suggests that a pusher-like swimmer such as *E. coli* might also exhibit negative viscotaxis. However, a detail calculation of the hydrodynamic torque on a rotating helix due to an imbalance in the viscosity that it experiences is still lacking, and therefore further investigation would be necessary to draw definite conclusions.

The idealized system considered in our paper was desiged to emulate biological processes, in particular the one by which bacteria are capable of penetrating mucus layers or membranes to cause infections. Even in the simplified situation considered in our paper the process is seen to exhibit rich dynamics. We hope that this study will motivate further work on swimming in viscosity-stratified fluids.

ACKNOWLEDGMENTS

We thank K. Dekkers for his help while conducting the experiments. J.G.-G. acknowledges the support of DGAPA-UNAM for postdoctoral financial support. This project has received funding from the European Research Council (ERC) under the European Union's Horizon 2020 research and innovation programme (grant agreement 682754 to E.L.).

C.E.L. and J.G.-G. contributed equally to this work.

[1] D. B. Dusenbery, *Living at Micro Scale: The Unexpected Physics of Being Small* (Harvard University Press, Cambridge, MA, 2009).

[2] G. Jékely, J. Colombelli, H. Hausen, K. Guy, E. Stelzer, F. Nédélec, and D. Arendt, Mechanism of phototaxis in marine zooplankton, Nature (London) **456**, 395 (2008).

[3] R. R. Bennett and R. Golestanian, A steering mechanism for phototaxis in *Chlamydomonas*, J. R. Soc. Interface **12**, 20141164 (2015).

[4] A. Giometto, F. Altermatt, A. Maritan, R. Stocker, and A. Rinaldo, Generalized receptor law governs phototaxis in the phytoplankton *Euglena gracilis*, Proc. Natl. Acad. Sci. USA **112**, 7045 (2015).

[5] C. Lozano, B. ten Hagen, H. Löwen, and C. Bechinger, Phototaxis of synthetic microswimmers in optical landscapes, Nat. Commun. **7**, 12828 (2016).

[6] B. Dai, J. Wang, Z. Xiong, X. Zhan, W. Dai, C.-C. Li, S.-P. Feng, and J. Tang, Programmable artificial phototactic microswimmer, Nat. Nanotechnol. **11**, 1087 (2016).

[7] S. Klumpp and D. Faivre, Magnetotactic bacteria, Eur. Phys. J. Spec. Top. **225**, 2173 (2016).

[8] J.-F. Rupprecht, N. Waisbord, C. Ybert, C. Cottin-Bizonne, and L. Bocquet, Velocity Condensation for Magnetotactic Bacteria, Phys. Rev. Lett. **116**, 168101 (2016).

[9] N. Waisbord, C. T. Lefèvre, L. Bocquet, C. Ybert, and C. Cottin-Bizonne, Destabilization of a flow focused suspension of magnetotactic bacteria, Phys. Rev. Fluids **1**, 053203 (2016).

[10] A. Bahat, I. Tur-Kaspa, A. Gakamsky, L. C. Giojalas, H. Breitbart, and M. Eisenbach, Thermotaxis of mammalian sperm cells: A potential navigation mechanism in the female genital tract, Nat. Med. **9**, 149 (2003).

[11] Y. Li, Y. Zhao, X. Huang, X. Lin, Y. Guo, D. Wang, C. Li, and D. Wang, Serotonin control of thermotaxis memory behavior in nematode *Caenorhabditis elegans*, PLoS ONE **8**, e77779 (2013).

[12] T. Bickel, G. Zecua, and A. Würger, Polarization of active Janus particles, Phys. Rev. E **89**, 050303 (2014).

[13] B. ten Hagen, F. Kümmel, R. Wittkowski, D. Takagi, H. Löwen, and C. Bechinger, Gravitaxis of asymmetric self-propelled colloidal particles, Nat. Commun. **5**, 4829 (2014).

[14] A. I. Campbell and S. J. Ebbens, Gravitaxis in spherical Janus swimming devices, Langmuir **29**, 14066 (2013).

[15] A. I. Campbell, R. Wittkowski, B. ten Hagen, H. Löwen, and S. J. Ebbens, Helical paths, gravitaxis, and separation phenomena for mass-anisotropic self-propelling colloids: Experiment versus theory, J. Chem. Phys. **147**, 084905 (2017).

[16] M. Eisenbach, *Chemotaxis* (World Scientific Publishing Company, Singapore, 2004).

[17] H. C. Berg, *E. coli in Motion* (Springer Science & Business Media, New York, 2008).

[18] J. D. Murray, *Mathematical Biology II: Spatial Models and Biomedical Applications* (Springer-Verlag, New York, 2003).

[19] J. T. Bonner and L. J. Savage, Evidence for the formation of cell aggregates by chemotaxis in the development of the slime mold *Dictyostelium discoideum*, J. Exp. Zool. **106**, 1 (1947).

[20] G. Gerisch, Cell aggregation and differentiation in *Dictyostelium*, in *Current Topics in Developmental Biology*, edited by A. A. Moscona and A. Monroy, Vol. 3 (Elsevier, New York, 1968), pp. 157–197.

[21] Z. Eidi, F. Mohammad-Rafiee, M. Khorrami, and A. Gholami, Modelling of *Dictyostelium discoideum* movement in a linear gradient of chemoattractant, Soft Matter **13**, 8209 (2017).

[22] E. F. Keller and L. A. Segel, Initiation of slime mold aggregation viewed as an instability, J. Theor. Biol. **26**, 399 (1970).

[23] E. F. Keller and L. A. Segel, Model for chemotaxis, J. Theor. Biol. **30**, 225 (1971).
[24] L. Laganenka, R. Colin, and V. Sourjik, Chemotaxis towards autoinducer 2 mediates autoaggregation in *Escherichia coli*, Nat. Commun. **7**, 12984 (2016).
[25] M. J. Daniels, J. M. Longland, and J. Gilbart, Aspects of motility and chemotaxis in spiroplasmas, Microbiology **118**, 429 (1980).
[26] G. E. Kaiser and R. N. Doetsch, Enhanced translational motion of *Leptospira* in viscous environments, Nature (London) **255**, 656 (1975).
[27] M. G. Petrino and R. N. Doetsch, Viscotaxis, a new behavioural response of Leptospira interrogans (biflexa) strain B16, J. Gen. Microbiol. **109**, 113 (1978).
[28] K. Takabe, H. Tahara, S. Islam, S. Affroze, S. Kudo, and S. Nakamura, Viscosity-dependent variations in the cell shape and swimming manner of *Leptospira*, Microbiology **163**, 153 (2017).
[29] P. Illien, R. Golestanian, and A. Sen, Fuelled motion: phoretic motility and collective behaviour of active colloids, Chem. Soc. Rev. **46**, 5508 (2017).
[30] P. Romanczuk, M. Bär, W. Ebeling, B. Lindner, and L. Schimansky-Geier, Active brownian particles, Eur. Phys. J. Spec. Top. **202**, 1 (2012).
[31] J. Elgeti, R. G. Winkler, and G. Gompper, Physics of microswimmers—Single particle motion and collective behavior: A review, Rep. Prog. Phys. **78**, 056601 (2015).
[32] S. A. Mirbagheri and H. C. Fu, *Helicobacter pylori* Couples Motility and Diffusion to Actively Create a Heterogeneous Complex Medium in Gastric Mucus, Phys. Rev. Lett. **116**, 198101 (2016).
[33] K. M. Ottemann and A. C. Lowenthal, *Helicobacter pylori* uses motility for initial colonization and to attain robust infection, Infect. Immun. **70**, 1984 (2002).
[34] E. Lauga, Bacterial hydrodynamics, Annu. Rev. Fluid Mech. **48**, 105 (2016).
[35] M. Laumann and W. Zimmermann, Focusing and splitting of particle streams in microflows via viscosity gradients, Eur. Phys. J. E **42**, 108 (2019).
[36] N. Oppenheimer, S. Navardi, and H. A. Stone, Motion of a hot particle in viscous fluids, Phys. Rev. Fluids **1**, 014001 (2016).
[37] B. Liebchen, P. Monderkamp, B. ten Hagen, and H. Löwen, Viscotaxis: Microswimmer Navigation in Viscosity Gradients, Phys. Rev. Lett. **120**, 208002 (2018).
[38] M. Yu Sherman, E. O. Timkina, and A. N. Glagolev, Viscosity taxis in *Escherichia coli*, FEMS Microbiol. Lett. **13**, 137 (1982).
[39] M. J. Lighthill, On the squirming motion of nearly spherical deformable bodies through liquids at very small Reynolds numbers, Commun. Pur. Appl. Math. **5**, 109 (1952).
[40] J. R. Blake, A spherical envelope approach to ciliary propulsion, J. Fluid Mech. **46**, 199 (1971).
[41] T. J. Pedley, Spherical squirmers: Models for swimming micro-organisms, IMA J. Appl. Math. **81**, 488 (2016).
[42] P. S. Eastham and K. Shoele, Axisymmetric squirmers in Stokes fluid with nonuniform viscosity, Phys. Rev. Fluids **5**, 063102 (2020).
[43] C. Datt and G. J. Elfring, Active Particles in Viscosity Gradients, Phys. Rev. Lett **123**, 158006 (2019).
[44] E. Lauga, *The Fluid Dynamics of Cell Motility* (Cambridge University Press, Cambridge, 2020).
[45] C. Bechinger, R. Di Leonardo, H. Löwen, C. Reichhardt, G. Volpe, and G. Volpe, Active particles in complex and crowded environments, Rev. Mod. Phys. **88**, 045006 (2016).
[46] M. J. Tindall, P. K. Maini, S. L. Porter, and J. P. Armitage, Overview of mathematical approaches used to model bacterial chemotaxis II: Bacterial populations, Bull. Math. Biol. **70**, 1570 (2008).
[47] M. Meyer, L. Schimansky-Geier, and P. Romanczuk, Active Brownian agents with concentration-dependent chemotactic sensitivity, Phys. Rev. E **89**, 022711 (2014).
[48] S. Saha, R. Golestanian, and S. Ramaswamy, Clusters, asters, and collective oscillations in chemotactic colloids, Phys. Rev. E **89**, 062316 (2014).
[49] O. Pohl and H. Stark, Self-phoretic active particles interacting by diffusiophoresis: A numerical study of the collapsed state and dynamic clustering, Eur. Phys. J. E **38**, 93 (2015).
[50] B. Liebchen, D. Marenduzzo, I. Pagonabarraga, and M. E. Cates, Clustering and Pattern Formation in Chemorepulsive Active Colloids, Phys. Rev. Lett. **115**, 258301 (2015).

[51] O. Pohl and H. Stark, Dynamic Clustering and Chemotactic Collapse of Self-Phoretic Active Particles, Phys. Rev. Lett. **112**, 238303 (2014).
[52] B. Liebchen, M. E. Cates, and D. Marenduzzo, Pattern formation in chemically interacting active rotors with self-propulsion, Soft Matter **12**, 7259 (2016).
[53] B. Liebchen, D. Marenduzzo, and M. E. Cates, Phoretic Interactions Generically Induce Dynamic Clusters and Wave Patterns in Active Colloids, Phys. Rev. Lett. **118**, 268001 (2017).
[54] L. Zhang, J. J. Abbott, L. Dong, B. E. Kratochvil, D. Bell, and B. J. Nelson, Artificial bacterial flagella: Fabrication and magnetic control, Appl. Phys. Lett. **94**, 064107 (2009).
[55] S. Gómez, F. A. Godínez, E. Lauga, and R. Zenit, Helical propulsion in shear-thinning fluids, J. Fluid Mech. **812**, R3 (2017).
[56] F. A. Godínez, L. Koens, T. D. Montenegro-Johnson, R. Zenit, and E. Lauga, Complex fluids affect low-Reynolds number locomotion in a kinematic-dependent manner, Exp. Fluids **56**, 97 (2015).
[57] J. Gonzalez-Gutierrez, S. Osorio-Ramirez, F. J. Solorio-Ordaz, and R. Zenit, Dynamics of a helical swimmer crossing an interface between two immiscible fluids, Phys. Rev. Fluids **4**, 083102 (2019).
[58] F. A. Godínez, O. Chávez, and R. Zenit, Note: Design of a novel rotating magnetic field device, Rev. Sci. Instrum. **83**, 066109 (2012).
[59] M. Mathlouthi and J. Génotelle, Rheological properties of sucrose solutions and suspensions, in *Sucrose* (Springer, New York, 1995), pp. 131–132.
[60] R. G. Cox, The motion of long slender bodies in a viscous fluid Part 1. General theory, J. Fluid. Mech. **44**, 791 (1970).
[61] H. See and M. Doi, *Introduction to Polymer Physics* (Oxford University Press, New York, 1996).
[62] S. Kim and J. S. Karrila, *Microhydrodynamics: Principles and Selected Applications* (Butterworth-Heinemann, Boston, 1991).
[63] V. A. Shaik and A. M. Ardekani, Far-field flow and drift due to particles and organisms in density-stratified fluids, Phys. Rev. E **102**, 063106 (2020).
[64] K. M. Taute, S. Gude, S. J. Tans, and T. S. Shimizu, High-throughput 3D tracking of bacteria on a standard phase contrast microscope, Nat. Commun. **6**, 8776 (2015).
[65] J. Taktikos, H. Stark, and V. Zaburdaev, How the motility pattern of bacteria affects their dispersal and chemotaxis, PLoS ONE **8**, e81936 (2013).
[66] J. D. Antani, A. X. Sumali, T. P. Lele, and P. P. Lele, Anisotropic random walks reveal chemotaxis signaling output in run-reversing bacteria, bioRxiv 2020.06.23.163667 (2020).
[67] G. C. Hansson, Role of mucus layers in gut infection and inflammation, Curr. Opin. Microbiol. **15**, 57 (2012).
[68] S. Coppola and V. Kantsler, Green algae scatter off sharp viscosity gradients, Sci. Rep. **11**, 399 (2021).
[69] M. R. Stehnach, N. Waisbord, D. M. Walkama, and J. S. Guasto, Viscophobic turning dictates microalgae transport in viscosity gradients, Nature Phys. **17**, 926 (2021).